Monthly Notices of the ROYAL ASTRONOMICAL SOCIETY

MNRAS **514,** 1606–1627 (2022) https://doi.org/10.1093/mnras/stac638
Advance Access publication 2022 March 15

The young HD 73583 (TOI-560) planetary system: two 10-$M_\oplus$ mini-Neptunes transiting a 500-Myr-old, bright, and active K dwarf

O. Barragán [1★] D. J. Armstrong [2,3] D. Gandolfi [4] I. Carleo,[5] A. A. Vidotto [6] C. Villarreal D'Angelo,[7] A. Oklopčić,[8] H. Isaacson,[9] D. Oddo,[10] K. Collins [11] M. Fridlund [6,12] S. G. Sousa [13] C. M. Persson,[12] C. Hellier,[14] S. Howell,[15] A. Howard,[9] S. Redfield [16] N. Eisner [1] I. Y. Georgieva,[17] D. Dragomir,[10] D. Bayliss [2] L. D. Nielsen [1,18] B. Klein [1] S. Aigrain,[1] M. Zhang,[19] J. Teske,[20] J. D. Twicken,[15,21] J. Jenkins,[15] M. Esposito,[22] V. Van Eylen [23] F. Rodler,[24] V. Adibekyan,[13,25] J. Alarcon,[24] D. R. Anderson,[2,3] J. M. Akana Murphy,[26†] D. Barrado,[27] S. C. C. Barros,[13,25] B. Benneke,[28] F. Bouchy,[18] E. M. Bryant,[2,3] R. P. Butler,[20] J. Burt,[29] J. Cabrera,[30] S. Casewell,[31] P. Chaturvedi,[22] R. Cloutier,[11‡] W. D. Cochran,[32] J. Crane,[33] I. Crossfield,[34] N. Crouzet,[35] K. I. Collins [36] F. Dai,[37,38] H. J. Deeg,[39,40] A. Deline,[18] O. D. S. Demangeon,[13,25] X. Dumusque,[18] P. Figueira,[13,41] E. Furlan,[42] C. Gnilka,[42] M. R. Goad,[31] E. Goffo,[4,22] F. Gutiérrez-Canales,[43] A. Hadjigeorghiou,[2,3] Z. Hartman,[44] A. P. Hatzes,[22] M. Harris,[10] B. Henderson,[31] T. Hirano,[45,46] S. Hojjatpanah,[47] S. Hoyer,[47] P. Kabáth,[48] J. Korth,[17] J. Lillo-Box,[49] R. Luque,[50] M. Marmier,[18] T. Močnik,[44] A. Muresan,[17] F. Murgas,[39,40] E. Nagel,[43] H. L. M. Osborne,[23] A. Osborn,[2,3] H. P. Osborn,[37,51] E. Palle,[39,40] M. Raimbault,[18] G. R. Ricker,[37] R. A. Rubenzahl,[19] C. Stockdale,[52] N. C. Santos,[13,25] N. Scott,[15] R. P. Schwarz,[53] S. Shectman,[33] M. Raimbault,[18] S. Seager,[37] D. Ségransan,[18] L. M. Serrano,[4] M. Skarka,[48,54] A. M. S. Smith,[31] J. Šubjak,[48,55] T. G. Tan,[56,57] S. Udry,[18] C. Watson,[58] P. J. Wheatley,[2,3] R. West,[2,3] J. N. Winn,[38] S. X. Wang,[59] A. Wolfgang[60] and C. Ziegler[61]

Affiliations are listed at the end of the paper

Accepted 2022 March 5. Received 2022 March 3; in original form 2021 October 22

ABSTRACT

We present the discovery and characterization of two transiting planets observed by *TESS* in the light curves of the young and bright ($V = 9.67$) star HD73583 (TOI-560). We perform an intensive spectroscopic and photometric space- and ground-based follow-up in order to confirm and characterize the system. We found that HD73583 is a young (∼500 Myr) active star with a rotational period of 12.08 ± 0.11 d, and a mass and radius of 0.73 ± 0.02 $M_\odot$ and 0.65 ± 0.02 $R_\odot$, respectively. HD 73583 b ($P_b = 6.3980420^{+0.0000067}_{-0.0000062}$ d) has a mass and radius of $10.2^{+3.4}_{-3.1}$ $M_\oplus$ and 2.79 ± 0.10 $R_\oplus$, respectively, which gives a density of $2.58^{+0.95}_{-0.81}$ g cm^{-3}. HD 73583 c ($P_c = 18.87974^{+0.00086}_{-0.00074}$ d) has a mass and radius of $9.7^{+1.8}_{-1.7}$ $M_\oplus$ and $2.39^{+0.10}_{-0.09}$ $R_\oplus$, respectively, which translates to a density of $3.88^{+0.91}_{-0.80}$ g cm^{-3}. Both planets are consistent with worlds made of a solid core surrounded by a volatile envelope. Because of their youth and host star brightness, they both are excellent candidates to perform transmission spectroscopy studies. We expect ongoing atmospheric mass-loss for both planets caused by stellar irradiation. We estimate that the detection of evaporating signatures on H and He would be challenging, but doable with present and future instruments.

Key words: techniques: photometric – techniques: radial velocities – planets and satellites: individual: HD 73583 (TOI-560) – stars: activity.

1 INTRODUCTION

Two of the most noticeable characteristics of the transiting exoplanet population are the so-called 'hot Neptunian desert' (Lundkvist et al. 2016; Mazeh, Holczer & Faigler 2016) and the 'radius valley' (Fulton et al. 2017; Van Eylen et al. 2018). Both correspond to regions with a lack of planets within certain ranges of planetary radii and stellar irradiance. Theoretical evolution models suggest that these gaps are mainly caused by physical mechanisms that occur during the first Myr of evolution (≲1 Gyr), such as photoevaporation (e.g. Adams & Laughlin 2006; Raymond et al. 2009; Owen & Wu 2013; Lopez & Fortney 2014; Kubyshkina et al. 2018; Mordasini 2020) and core-

★ E-mail:oscar.barragan@physics.ox.ac.uk
† NSF Graduate Research Fellow.
‡ Banting Fellow.

powered mass-loss (e.g. Ginzburg, Schlichting & Sari 2016; Gupta & Schlichting 2019, 2021).

Young exoplanets (<1 Gyr) offer us snapshots of early planetary evolution that can be used to test the role of diverse physical mechanisms sculpting exoplanet populations. The few well-characterized young exoplanets have given us some insights on the role of photoevaporation in early exoplanet evolution. One of them is K2-100 b (∼750 Myr), a young and highly irradiated exoplanet that lies on the border of the hot Neptunian desert (Mann et al. 2017). Recent studies suggest that the planet is currently evaporating and its radius will be significantly smaller in a few Gyr, which will eventually cause it to leave the hot Neptunian desert (Barragán et al. 2019). Another example is the AU Mic b (∼22 Myr) planet (Plavchan et al. 2020; Cale et al. 2021; Klein et al. 2021; Szabó et al. 2021), whose density is consistent with a planet with a thick volatile envelope that may be evaporating (e.g. Carolan et al. 2020).

The Transiting Exoplanet Survey Satellite (*TESS*; Ricker et al. 2015) has discovered a plethora of candidates/exoplanets transiting bright stars (e.g. Newton et al. 2019, 2021; Bouma et al. 2020; Plavchan et al. 2020; Rizzuto et al. 2020; Hobson et al. 2021; Kossakowski et al. 2021; Mann et al. 2021; Martioli et al. 2021; Zhou et al. 2021). These transiting exoplanets are excellent targets to perform follow-up observations that allow us to further characterize these young systems, e.g. using the radial velocity (RV) method to measure the planetary masses. However, detecting the planetary signatures in RV time-series of young stars is challenging due to their inherent activity. Active regions on stellar surfaces induce an apparent RV shift that can mimic or hide planetary signals (e.g. Queloz et al. 2001b; Huélamo et al. 2008; Rajpaul, Aigrain & Roberts 2016; Faria et al. 2020). Therefore, in order to detect the planetary signals in stellar RVs, state-of-the-art spectrographs are not enough and we need to use techniques tailored to disentangle planetary and stellar signals in our RV data (see Hatzes et al. 2010, 2011; Haywood et al. 2014; Grunblatt, Howard & Haywood 2015; Rajpaul et al. 2015; e.g. Barragán et al. 2018). This is especially important for exoplanets with expected RV signals of the order of a few m s^{-1}, which is similar to (or smaller than) the stellar signals of some young active stars (e.g. Barragán et al. 2019; Lillo-Box et al. 2020; Kossakowski et al. 2021).

In this paper, we present the discovery and mass measurement of two mini-Neptunes transiting HD 73583 (TOI-560, TIC 101011575), a young star observed by *TESS* in Sectors 8 and 34. HD 73583 is a relatively bright ($V = 9.67$) and high proper motion star located in the Southern hemisphere. Table 1 shows the main identifiers for HD 73583. The characterization of this system is part of the *KESPRINT* (e.g. Gandolfi et al. 2018, 2019; Esposito et al. 2019; Carleo et al. 2020; Georgieva et al. 2021) and *NCORES* (e.g. Armstrong et al. 2020; Nielsen et al. 2020; Osborn et al. 2021) consortia, which have discovered and characterized several *TESS* exoplanets. This manuscript is organized as follows: In Section 2, we describe the *TESS* observations. Section 3 is devoted to the description of our intensive photometric and spectroscopic follow-up of the star. Sections 4 and 5 describe our stellar and planetary data analyses, respectively. We close in Section 6 with our discussion and conclusions.

Table 1. Main identifiers, coordinates, proper motion, parallax, and optical and infrared magnitudes of HD 73583.

Parameter	Value	Source
Main identifiers		
TIC	101011575	TIC[a]
Gaia DR2	5746824674801810816	TIC[a], *Gaia*[b]
TYC	5441-00431-1	TIC[a]
2MASS	J08384526-1315240	TIC[a]
Spectral type	K4V	Gray et al. (2006)
Equatorial coordinates, proper motion, and parallax		
α(J2000.0)	08 38 45.26042	TIC[a], *Gaia*[b]
δ(J2000.0)	−13 15 24.0910	TIC[a], *Gaia*[b]
μ_α (mas yr^{-1})	-63.8583 ± 0.050515	TIC[a], *Gaia*[b]
μ_δ (mas yr^{-1})	38.3741 ± 0.040586	TIC[a], *Gaia*[b]
π (mas)	31.6501 ± 0.0319	Gaia[b]
Distance (pc)	31.60 ± 0.032	This work
Magnitudes		
TESS	8.5925 ± 0.006	TIC[a]
Gaia	9.27033 ± 0.00048	TIC[a], *Gaia*[b]
B	10.742 ± 0.07	TIC[a]
V	9.67 ± 0.03	TIC[a]
J	7.649 ± 0.026	Cutri et al. (2003)
H	7.092 ± 0.051	Cutri et al. (2003)
Ks	6.948 ± 0.024	Cutri et al. (2003)
W1	6.85 ± 0.037	Wright et al. (2010)
W2	6.963 ± 0.021	Wright et al. (2010)
W3	6.921 ± 0.017	Wright et al. (2010)
W4	6.723 ± 0.084	Wright et al. (2010)

Notes.[a]TESS Input Catalog (TIC; Stassun et al. 2018, 2019).
[b]Gaia Collaboration (2018).

2 *TESS* PHOTOMETRY

TESS observed HD 73583 (TOI-560, TIC 101011575) in Sector 8 from 2019 February 2 to 2019 February 28 on camera 2 with a cadence of 2 min. The *TESS* Science Processing Operations Center (SPOC; Jenkins et al. 2016) transit search (Jenkins 2002; Jenkins et al. 2010, 2020) discovered a transiting signal with a period of 6.4 d in HD 73583's light curve. This was announced in the *TESS* SPOC Data Validation Report (DVR; Twicken et al. 2018; Li et al. 2019),[1] and designated by the TESS Science Office as TESS Object of Interest (TOI; Guerrero et al. 2021) TOI-560.01 (hereafter HD 73583 b). We identified HD 73583 as a good candidate and we started an intensive follow-up to further characterize the nature of this system (See Section 3). Fig. 1 shows the sector 8 normalized Presearch Data Conditioning Simple Aperture Photometry (PDCSAP; Smith et al. 2012; Stumpe et al. 2012, 2014) light curve for HD 73583 as downloaded from the Mikulski Archive for Space Telescopes (MAST). We note that Sector 8 has a relatively large data gap of more than 5 d. This was caused by an interruption in communications between the instrument and spacecraft that resulted in no collection of data during this time.[2]

Two years later, *TESS* reobserved HD 73583 as part of its extended mission in Sector 34 between 2021 January 13 and 2021 February 9 in camera 2 with a 2-min cadence. We downloaded the Sector 34 HD 73583's light curve from the MAST archive. We found that the expected transit signals associated with HD 73583 b were consistent with the transits observed in Sector 8. We also detected by eye two extra transits in Sector 34 that do not have a counterpart in Sector 8 at times 2232.17 and 2251.06 BTJD, where BTJD = BJD − 2457 000 is the Barycentric *TESS* Julian date. These two new transits have similar depths (∼1130 ppm), suggesting that they are caused by the

[1]DVR for HD 73583 b can be found in this link.
[2]Sector 8 release notes can be found in this link.

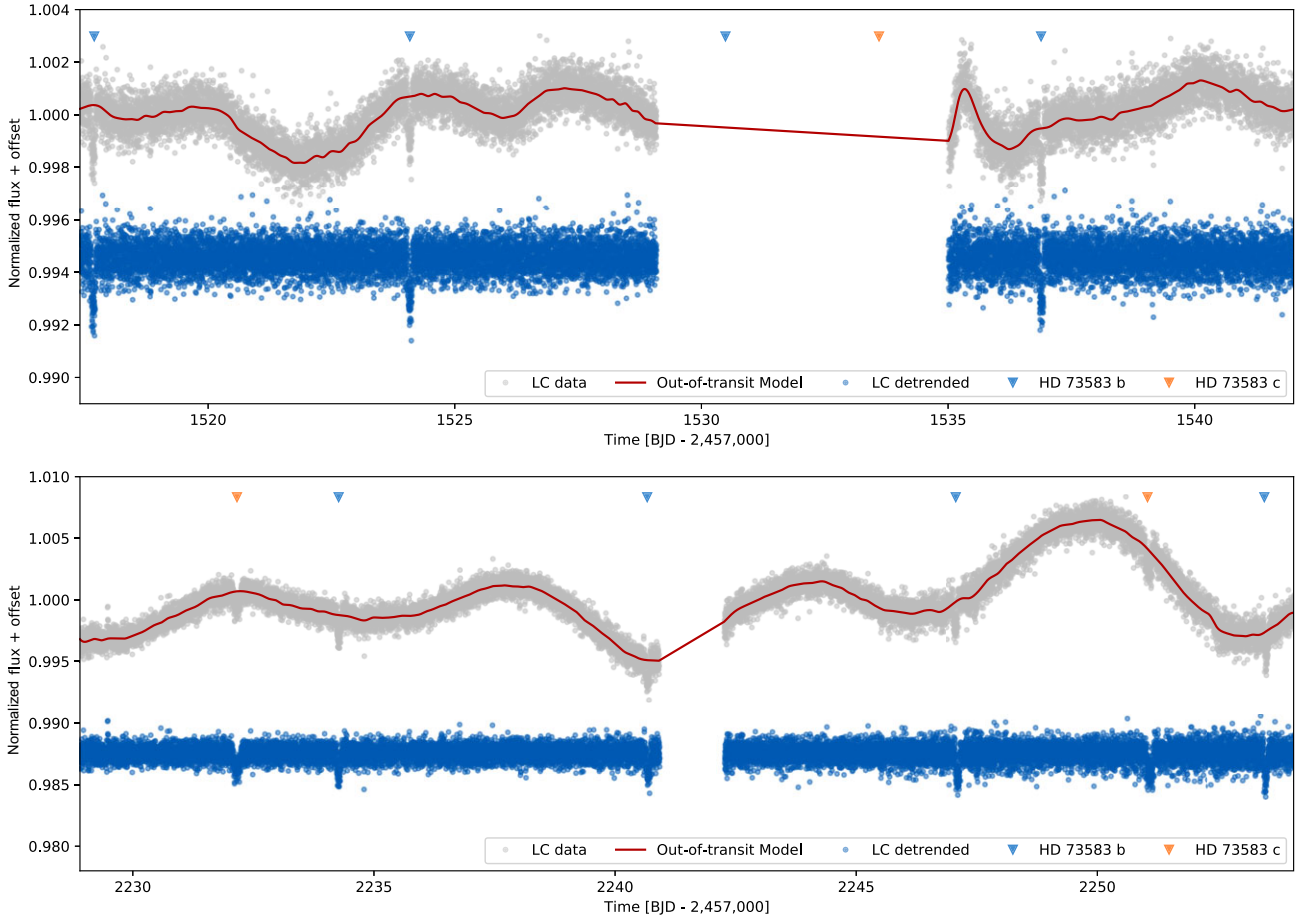

Figure 1. *TESS*'s Sector 8 (upper panel) and Sector 34 (lower panel) light curves for HD 73583. *TESS* data are shown with grey points with the out-of-transit variability model overplotted in red. The resulting flattened light curves are shown with blue points. Transit positions are marked with blue and orange triangles for HD 73583 b and HD 73583 c, respectively.

same transiting object with a period of 18.9 d. At this point, we had enough spectroscopic data to test a planetary origin of the signal. We performed a preliminary analysis and detected a Doppler signal in our RVs consistent with the 18.9-d period (See Section 5 for the full details on the RV analysis), suggesting that these transits have a planetary origin. Hereafter we refer to this signal as HD 73583 c. The reason why there is no HD 73583 c's transit signal in Sector 8 is because the expected transit time coincides with the relatively long data gap (see Fig. 1). HD 73583 c was also announced as a Community TOI (CTOI) and TOI in the EXOFOP website as TOI-560.02. Both TOIs were detected with the correct ephemerides in the SPOC transit search of the combined data for sectors 8 and 34 (Guerrero et al. 2021).

We note that the Sector 34 PDCSAP light curve shows significantly systematic variations, especially during the second half of the observations. According to *TESS*' Sector 34 release notes, orbit 76 suffered from significant spacecraft motion.[3] This suggests that the apparent PDCSAP light-curve corruption is likely caused by an overfitting of the Cotrending Base Vectors (CBVs) when trying to correct the significant spacecraft motion. For this reason we decided to perform our own light-curve correction using the `lightkurve` software (Lightkurve Collaboration 2018). Briefly, we use the `CBVCorrector` class to perform a 'Single-scale' and 'Spike' CBV correction. We first set a regularization term `alpha` $=1 \times 10^{-4}$. This produces a corrected light curve that is visibly similar to the PDCSAP one with an overfitting metric of 0.5 that is smaller than the recommended threshold of 0.8.[4] We therefore perform a scan over different values of the regularization term that provides an optimal overfitting and underfitting metric. We found that the best regularization term is `alpha` $=9.4 \times 10^{3}$. This implies a small correction of the original light curve by the CBVs, and the corrected data are practically identical to the SAP light curve. We therefore perform a 'Spike' only CBV correction (to only correct for short impulsive spike systematics) with a a regularization term `alpha` $= 1 \times 10^{-4}$. This generates a corrected light curve with an overfitting metric of 0.83 and underfitting metric of 0.91. These values are above the recommended values, and we therefore use this as our corrected light curve for Sector 34. To finish the light-curve processing we performed a crowding correction to account for extra flux that may be present in the SAP mask. We use the values given in the target pixel file to account and correct for the light curve

[3]Sector 34 release notes can be found in this link.

[4]For more details about CBV correction of *TESS* data see https://docs.lightkurve.org/tutorials/2-creating-light-curves/2-3-how-to-use-cbvcorrector.html.

contamination of ∼4 per cent.[5] Fig. 1 shows our processed Sector 34 light curve for HD 73583.

Astrophysical and instrumental false positives are very common in *TESS* data, in part due to the large pixel scale of 21 arcsec. We therefore performed standard diagnostic tests to help rule out false positive scenarios using the open-source Lightcurve Analysis Tool for Transiting Exoplanets (LATTE; Eisner, Lintott & Aigrain 2020). The tests to check for instrumental false positives include ensuring that the transit events do not coincide with the periodic momentum dumps and assessing the x and y centroid position around the time of the events. Similarly, tests for astrophysical false positives include assessing the background flux; examining the light curves of nearby stars observed by *TESS*; examining light curves extracted for each pixel around the target; and comparing the average in-transit with the average out of-transit flux. These tests increased our confidence that none of the transit signals are the result of systematic effects, such as a temperature change in the satellite, or that they are astrophysical false positives such as background eclipsing binaries or a Solar system object passing through the field of view.

HD 73583's *TESS* light curves show out-of-transit variability likely caused by activity regions on the stellar surface and/or instrumental systematics. For further transit analysis in this manuscript, we chose to remove the low-frequency trends in order to work with flattened light curves. We detrended the *TESS* light curves using the public code `citlalicue` (Barragán et al. 2022). Briefly, `citlalicue` uses Gaussian Processes (GPs) as implemented in `george` (Ambikasaran et al. 2015) to model the out-of-transit variability in the light curves. We fed `citlalicue` with the normalized light curves and we input the ephemeris of the two transiting signals. Since we are interested in removing the low-frequency signals, we bin the data to 3 h bins and mask out all the transits from the light curve when fitting the GP using a Quasi-Periodic kernel (as described in Ambikasaran et al. 2015). We use an iterative maximum Likelihood optimization together with a 5σ clipping algorithm to find the optimal model describing the out-of-transit light-curve variations. We then divide the whole light curves by the inferred model to obtain a flattened light curve containing only transit signals. We note that we detrended each *TESS* sector independently. Fig. 1 shows the detrended light curves for both *TESS* sectors. In Section 5, we present the modelling of the flattened *TESS* transits.

3 FOLLOW-UP OBSERVATIONS

3.1 High-resolution speckle imaging

Spatially close stellar companions can create a false-positive transit signal if, for example, the fainter star is an eclipsing binary. However, even more troublesome is 'third-light' flux contamination from a close companion (bound or line of sight) which can lead to underestimated derived planetary radii if not accounted for in the transit model (e.g. Ciardi et al. 2015) and even cause total non-detection of small planets residing within the same exoplanetary system (Lester et al. 2021). Thus, to search for close-in bound companions to exoplanet host stars that are unresolved in *TESS* or other ground-based follow-up observations, we obtained high-resolution imaging speckle observations of HD 73583.

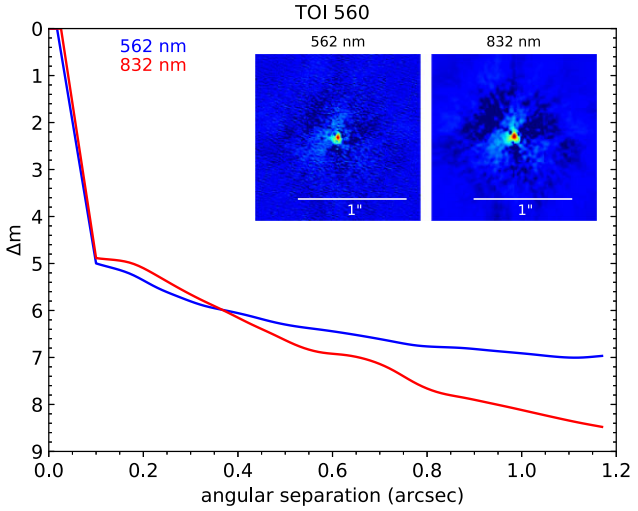

Figure 2. Contrast curves showing the 5σ detection sensitivity obtained using Zorro on Gemini with the filters centred on 562 nm (blue line) and 832 nm (red line). No bright companions are detected within 1.2 arcsec to HD 73583.

HD 73583 was observed twice, on 2020 March 16 and 2019 May 22 UT, using the Zorro speckle instrument on the Gemini South 8-m telescope.[6] The 2020 March observations will be discussed herein as the 2019 May observations had poorer seeing and worse sky conditions, however giving similar results to those obtained in 2020 March. Zorro provides simultaneous speckle imaging in two bands (562 and 832 nm) with output data products including a reconstructed image with robust contrast limits on companion detection (e.g. Howell et al. 2016).

Three sets of 1000 × 0.06 s exposures were collected for TOI 560 and subjected to Fourier analysis in our standard reduction pipeline (see Howell et al. 2011). Fig. 2 shows our final 5σ contrast curves and the reconstructed speckle images. We find that HD 73583 is single to within the contrast limits achieved by the observations, with no companion brighter than 5–8 mag below that of the target star found from the diffraction limit (20 mas) out to 1.2 arcsec. At the distance of HD 73583 these angular limits correspond to spatial limits of 0.6 to 37 AU.

3.2 *CHEOPS* observations

We observed HD 73583 with the CHaracterising ExOPlanet Satellite (*CHEOPS*; Benz et al. 2021) as part of our Guest Observer program (OBS ID 1345790) between 2021-01-26 UTC 01:40 and 2021-01-26 UTC 06:39, so as to capture a full transit of HD 73583 b with its precise photometry. *CHEOPS* is an ESA small-class mission with ultra-high-precision photometry dedicated to follow-up of stars with known planets. It conducts observations from a Sun-synchronous, low-Earth orbit, which in many cases leads to interruptions in on-target observations due to Earth occultations and crossings of the South Atlantic Anomaly (SAA) region. As such, each *CHEOPS* observation is associated with some observing efficiency, which is the fraction of time on target not interrupted by Earth occultation and SAA. We obtained one visit on the target at a relatively high efficiency of 72.7 per cent for a duration of 4.99 h. *CHEOPS* observations were then passed through the CHEOPS Data Reduction Pipeline

[5] See https://heasarc.gsfc.nasa.gov/docs/tess/UnderstandingCrowding.html for more details on *TESS* crowding correction.

[6] https://www.gemini.edu/sciops/instruments/alopeke-zorro/

Table 2. Summary of ground-based photometric follow-up observations.

Telescope	Location	Date [UTC]	Filter	Coverage
HD 73583 b				
NGTS 0.2 m	Chile	2019-12-06	NGTS	full
PEST 0.3m	Australia	2020-01-14	R_c	full
LCO-SAAO 1m	South Africa	2020-02-02	z-short	full
LCO-SSO 1m	Australia	2020-03-31	B	full
LCO-SAAO 1m	South Africa	2020-12-05	z-short	full
HD 73583 c				
LCO-CTIO 1m	Chile	2021-04-03	z-short	ingress
LCO-McDonald 1m	USA	2021-04-22	z-short	egress
LCO-McDonald 1m	USA	2021-04-22	z-short	egress

(DRP; Hoyer et al. 2020), which conducts calibration, correction, and photometry, as shown in the Data Reduction Report for each observation. We chose to use the 'OPTIMAL' light curve as provided by the DRP, which calculates optimal aperture size by maximizing the SNR based on field-of-view simulations to account for potential contaminant field stars. In this case, the 'OPTIMAL' aperture size was 26.0 pix, whereas the 'DEFAULT' aperture size was 25 pix.

The light curve was then detrended using the `pycheops` Python package (Maxted et al., submitted). We detrended the *CHEOPS* light curve to remove spacecraft motion, background noise, and Moon glint. In an effort to avoid overfitting, we tested whether the addition of a new detrending parameter was supported by the data by calculating the Bayes Factor of the model with/without the parameter one-by-one, and eliminating those parameters whose Bayes Factors $\geq$1. We use this detrended light curve for our analyses described in Section 5.

3.3 Ground-based transit observations

We conducted ground-based photometric follow-up observations as part of the *TESS* Follow-up Observing Program (TFOP; Collins et al. 2018). We used the `TESS Transit Finder`, which is a customized version of the `Tapir` software package (Jensen 2013), to schedule our transit observations. A summary of the observations is provided in Table 2.

We observed a full transit event of HD 73583 b simultaneously using four Next-Generation Transit Survey (NGTS; Wheatley et al. 2018) 0.2 m telescopes located at ESO's Paranal Observatory, Chile. Each NGTS telescope has an 8 square degree field of view and a plate scale of 5 arcsec pixel^{-1}. The observations were taken using a custom NGTS filter (520–890 nm) with 10 s exposure times and at airmass $<$1.95. Each telescope independently observed the transit event in the multitelescope operational mode as described in Bryant et al. (2020) and Smith et al. (2020). The NGTS data were reduced using a custom aperture photometry pipeline (Bryant et al. 2020), which uses the SEP library for both source extraction and photometry (Bertin & Arnouts 1996; Barbary 2016).

We observed a full transit of HD 73583 b from the Perth Exoplanet Survey Telescope (PEST) near Perth, Australia. The 0.3 m telescope is equipped with a 1530 $\times$ 1020 SBIG ST-8XME camera with an image scale of 1.″2 pixel^{-1} resulting in a 31 arcsec $\times$ 21 arcsec field of view. A custom pipeline based on `C-Munipack`[7] was used to calibrate the images and extract the differential photometry.

[7]http://c-munipack.sourceforge.net

We observed three full transits of HD 73583 b and one ingress and two simultaneous egresses of HD 73583 c from the Las Cumbres Observatory Global Telescope (LCOGT; Brown et al. 2013) 1.0 m network. The 4096 $\times$ 4096 LCOGT SINISTRO cameras have an image scale of 0.″389 per pixel, resulting in a 26 arcmin $\times$ 26 arcmin field of view. The images were calibrated by the standard LCOGT `BANZAI` pipeline (McCully et al. 2018), and photometric data were extracted with `AstroImageJ` (Collins et al. 2017).

3.4 RV follow-up

3.4.1 HARPS

We acquired 90 high-resolution (R $\approx$ 115 000) spectra with the High Accuracy Radial Velocity Planet Searcher (HARPS; Mayor et al. 2003) spectrograph mounted at the 3.6 m ESO telescope at La Silla Observatory. HARPS observes in the visible spectrum within the wavelength range of 380 to 690 nm. The typical exposure time per observation was 1500 s, which produced spectra with a typical S/N of 70–80 at 550 nm. The observations were carried out between 2019 April and 2020 March, as part of the two large observing programs 1102.C-0923 (PI: Gandolfi) and 1102.C-0249 (PI: Armstrong), and the ESO programs 60.A-9700 and 60.A-9709. We reduced the data using the dedicated HARPS data reduction software (DRS) and extracted the RV measurements by cross-correlating the Echelle spectra with a K5 numerical mask (Baranne et al. 1996; Pepe et al. 2002; Lovis & Pepe 2007). We also used the `DRS` to extract the Ca II H and K lines activity indicator (S_{HK}), and three profile diagnostics of the cross-correlation function (CCF), namely, the contrast, the full width at half-maximum (FWHM), and the bisector inverse slope (BIS). Our HARPS RV measurements have a typical error bar of 1.2 m s^{-1} and an RMS of 9.1 m s^{-1}. Table B1 lists the HARPS RV and activity indicators measurements.

We acknowledge that there are eight archival HARPS observations of HD 73583 taken in 2004 and 2005 (program: 072.C-0488, PI: Mayor). We note that the stellar activity may have changed significantly in the last 15 yr, and that those observations have a sub-optimal sampling. Therefore, we do not include them in our time-series analysis.

3.4.2 PFS

Teske et al. (2021) performed spectroscopic follow-up observations of HD 73583 as part of the Magellan-TESS Survey, which uses the Planet Finder Spectrograph (PFS; Crane et al. 2010) on the 6.5 m Magellan II telescope at Las Campanas Observatory in Chile. PFS covers wavelengths from 391 to 734 nm. 26 high-resolution (R $\approx$ 130 000) spectra were acquired between 2019 April 8 and 2019 May 24 UT. The typical integration time for each observation was 1200 s. These RVs measurements have a typical error bar of 0.8 m s^{-1} and an RMS of 6.3 m s^{-1}. We decided to include the PFS measurements in our spectroscopic time-series analysis given that they overlap with our HARPS observations. The table containing the Doppler and S-index measurements are available in electronic format in Teske et al. (2021).

3.4.3 HIRES

We collected 14 iodine-in observations and two template observations of HD 73583 between 2019 October 20 and 2020 January 1. Each spectrum was taken with the B5 decker with width 0.86 arcsec and height of 3.5 arcsec, resulting in resolution of approximately

60 000. The iodine-out observations that serve as in the RV forward model consist of two back-to-back observations of SNR ∼200 each. The median observation time of the iodine in observations is 560 s resulting in SNR ∼300 at 550 nm, the middle of the iodine cell absorption region. The set-up and data reduction follow the standard procedure laid out in Howard et al. (2010). RVs have a median internal error of 1.0 m s^{-1} and pre-fit RMS of 12.2 m s^{-1}. The RV errors from HIRES for this young star are higher than they would be for a solar-aged star. Table B2 shows the HIRES RV and $S_{\rm HK}$ measurements.

3.4.4 CORALIE

HD 73583 was observed with the CORALIE high-resolution echelle spectrograph on the 1.2 m Euler telescope at La Silla Observatory (Queloz et al. 2001a). The star was part of a blind RV survey for planets around K-dwarfs within 65 pc. In total 17 spectra were obtained between 2016-09-24 and 2017-12-04 UT. One observation was discarded from further analysis due to abnormal instrument drift during the exposure. RVs were extracted via cross-correlation with a binary G2 mask (Baranne et al. 1996), using the standard CORALIE data-reduction pipeline. We also derived cross-correlation (CCF) line-diagnostics such as bisector-span and FWHM to check for possible false-positive scenarios (Queloz et al. 2001b). We obtained a typical SNR of 50 that, together with intrinsic signals in the data, gives a RV precision of 5–7 m s^{-1} and an RMS of the measurements of 12 m s^{-1}. The Ca II index was computed using the usual prescription. Table B3 shows the CORALIE spectroscopic observations.

4 STELLAR DATA ANALYSIS

4.1 Spectroscopic parameters

We used the HARPS observations to produce a high signal-to-noise (S/N = 700 at 550 nm) spectrum of HD 73583. Briefly, we arbitrarily chose one of the RV observations as the zero velocity and through a cross-correlation procedure shift and add all the other observations to this one. Because of the inherent lack of accuracy in *all* available methods, we use three independent methods in order to derive the basic three spectroscopic parameters: effective temperature ($T_{\rm eff}$), surface gravity ($\log g$), and metallicity ([Fe/H]).

The first method, using `SpecMatch-Emp` (Yee, Petigura & von Braun 2017), compares a standardized version of our spectrum to a library of more than 400 spectra of stars with well-determined parameters. Through interpolation and a minimizing process the code provides a set of stellar fundamental parameters such as $T_{\rm eff}$, metallicity ([Fe/H]), $\log g$. `SpecMatch-Emp` also provides estimates of the stellar mass and radius by comparing with stellar masses and radii for stars in the sample during the minimization process. Table 3 shows the main spectroscopic parameters for HD 73583 obtained with `SpecMatch-Emp`.

Our second method is utilizing the code `SME` (Spectroscopy Made Easy; Piskunov & Valenti 2017), a well-proven tool for determining stellar parameters using synthetic spectra. By providing some basic information about the observed spectrum, such as estimates of the fundamental stellar parameters $T_{\rm eff}$, $\log g$, [Fe/H], $v \sin i$, $v_{\rm mac}$, or $v_{\rm mic}$ together with atomic or molecular line data from the VALD3 data base (Piskunov et al. 1995; Kupka et al. 1999), one can fit the observed spectrum. Calling a dynamically linked external library of models, `SME` performs a synthesis of the stellar atmospheric spectrum. Functions in the library solve for molecular and ionization equilibrium, continuous and line opacities, calculating spectra while solving for the parameters left free. Using an iterative scheme, varying one or two fundamental parameters at a time, and with the inherent chi-square minimizing technique, `SME` eventually arrives at the most appropriate parameters for the model best fitting the observed spectrum. Table 3 shows the main spectroscopic parameters obtained with `SME`.

Our third method uses `ARES + MOOG`, following the same methodology described in Santos et al. (2013), Sousa (2014), and Sousa et al. (2021). We used the combined spectrum to derive the equivalent widths of iron lines using the `ARES` code[8] (Sousa et al. 2007, 2015). We used a minimization process to find ionization and excitation equilibrium and converge to the best set of spectroscopic parameters. This process makes use of a grid of Kurucz (1993) model atmospheres and the radiative transfer code `MOOG` (Sneden 1973). Following the same methodology as described in Sousa et al. (2021), we used the GAIA eDR3 *Gaia* parallax and estimated the trigonometric surface gravity to be 4.60 ± 0.06 dex. Table 3 shows a summary with our `ARES + MOOG` results.

4.2 Stellar mass and radius

Our three methods to retrieve stellar spectroscopic parameters provide results that agree well within the uncertainties (Table 3). We decide to adopt the `SpecMatch-Emp` parameters for further analyses given that this method provides the most conservative error bars. We then use the `SpecMatch-Emp` spectroscopic stellar parameters together with `PARAM 1.3`[9] (da Silva et al. 2006) with the `PARSEC` isochrones (Bressan et al. 2012) to derive HD 73583's mass and radius. We use the $T_{\rm eff}$ and [Fe/H] from our `SpecMatch-Emp` analysis together with the visual magnitude and parallax given in Table 1 as input for `PARAM 1.3`. Given the expected youth of the star, we set stellar age priors between 0.1 and 1 Gyr (See Section 4.4). Table 3 shows HD 73583's parameters obtained with `PARAM 1.3`. We note that these parameters are in full agreement within 1σ with the mass and radius estimated using `SpecMatch-Emp`.

As an extra check to our stellar mass and radius determination, we also perform a spectral energy distribution (SED) modelling using the software `ARIADNE` (Acton et al. 2020). Grids of four stellar atmospheric models, `Phoenix v2` (Husser et al. 2013), `BtSettl` (Allard, Homeier & Freytag 2012), Castelli & Kurucz (2004), and Kurucz (1993) were interpolated with priors for $T_{\rm eff}$, $\log g_\star$, [Fe/H] from `SpecMatch-Emp` (Table 3). Stellar radius, distance, and extinction (A_V) were treated as free parameters. We used broad-band photometry from 2MASS J, H, and K, *WISE* W1 and W2, the *Johnson* B and V magnitudes from APASS, and *Gaia* G, $G_{\rm BP}$, and $G_{\rm RP}$ magnitudes and parallax from eDR-3. An upper limit to the extinction was taken from the maximum line-of-sight value from the dust maps of Schlegel, Finkbeiner & Davis (1998). Bayesian Model Averaging was used to compute the final stellar radius which was found to be $0.693^{+0.019}_{-0.028}$ $R_\odot$. `ARIADNE` also computed the stellar mass using MIST (Choi et al. 2016) stellar evolution tracks to $0.727^{+0.022}_{-0.030}$ $M_\odot$. These results agrees within 1σ with the above derived mass and radius from `PARAM 1.3`. Fig. 3 shows the SED fit obtained with `ARIADNE`, and the corresponding results are summarized in Table 3.

[8]The last version of ARES code (ARES v2) can be downloaded at http://www.astro.up.pt/∼sousasag/ares

[9]http://stev.oapd.inaf.it/cgi-bin/param_1.3.

Table 3. HD 73583's parameters. The adopted parameters for the rest of the manuscript are marked with boldface.

Parameter	SpecMatch-Emp	SME	ARES + MOOG	PARAM1.3	ARIADNE	stardate	time-log R'_{HK}	WASP
T_{eff} (K)	**4511 ± 110**	4532 ± 80	4555 ± 99	–	–	–	–	–
log g (cgs)	**4.62 ± 0.12**	4.42 ± 0.08	4.60 ± 0.06	4.63 ± 0.02	–	–	–	–
[Fe/H] (dex)	**0.00 ± 0.09**	0.00 ± 0.05	−0.132 ± 0.053	–	–	−0.02 ± 0.06	–	–
$v \sin i$	–	3.5 ± 0.5	–	–	–	–	–	–
Mass ($M_\odot$)	0.72 ± 0.08	–	–	**0.73 ± 0.02**	$0.727^{+0.022}_{-0.030}$	0.74 ± 0.02	–	–
Radius ($R_\odot$)	0.70 ± 0.10	–	–	**0.65 ± 0.02**	$0.693^{+0.019}_{-0.030}$	–	–	–
Density (g cm^{-3})	$2.9^{+1.8}_{-1.0}$	–	–	**3.75 ± 0.38**	$3.08^{+0.46}_{-0.39}$	–	–	–
Age (Gyr)	–	–	–	0.44 ± 0.33	–	0.750 ± 0.020	**0.48 ± 0.19**	–
Rotation period (d)	–	–	–	–	–	–	–	12.2 ± 0.2

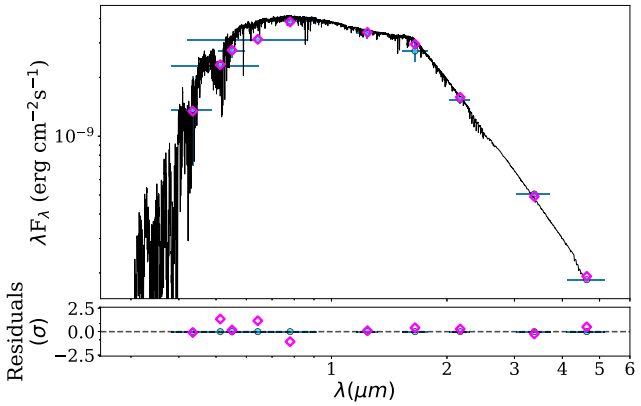

Figure 3. The SED of HD 73583 and the model calculated from the model grid with the highest probability. The magenta points are the synthetic photometry and the blue points the observed photometry where the vertical errors mark the 1σ uncertainties and the horizontal bars the effective width of the pass-bands. The residuals in the lower panel are normalized to the errors of the photometry.

As a further check on the reliability of our stellar parameters, we also performed some basic checks within our exoplanet analyses (see Section 5). We compare the planetary surface gravity obtained from the derived planet masses and radii (that depends on the derived stellar mass and radius) with the value obtained from the scaled parameters (that do not depend on the stellar mass and radius, see Southworth, Wheatley & Sams 2007). Both values for both planets are in agreement within <0.1σ (see Section 5). These results suggest that the derived stellar parameters in this section are reliable.

4.3 Stellar rotation period

We note that *TESS* photometry shows flux modulation in both HD 73583's light curves (see Section 2 and Fig. 1). These are likely caused by active regions on the stellar surface. Fortunately, they can be a proxy to estimate the stellar rotation period. A Fourier transform of Sector 8 and 34 light curves shows peaks at ∼12 and ∼6 d, being the later likely the first harmonic caused by a complex distribution of spots in the stellar surface. Given that the *TESS* observations cover only approximately two rotational period of the star, we decide to use ground-base photometry that expands for a longer time window to estimate a more precise stellar rotational period.

HD 73583 was observed with the WASP-South (Pollacco et al. 2006) camera array over 100-night spans in four consecutive years from 2009 to 2012, accumulating 17 000 photometric observations. The 200-mm, f/1.8 lenses were backed by a 2048x2048 CCDs

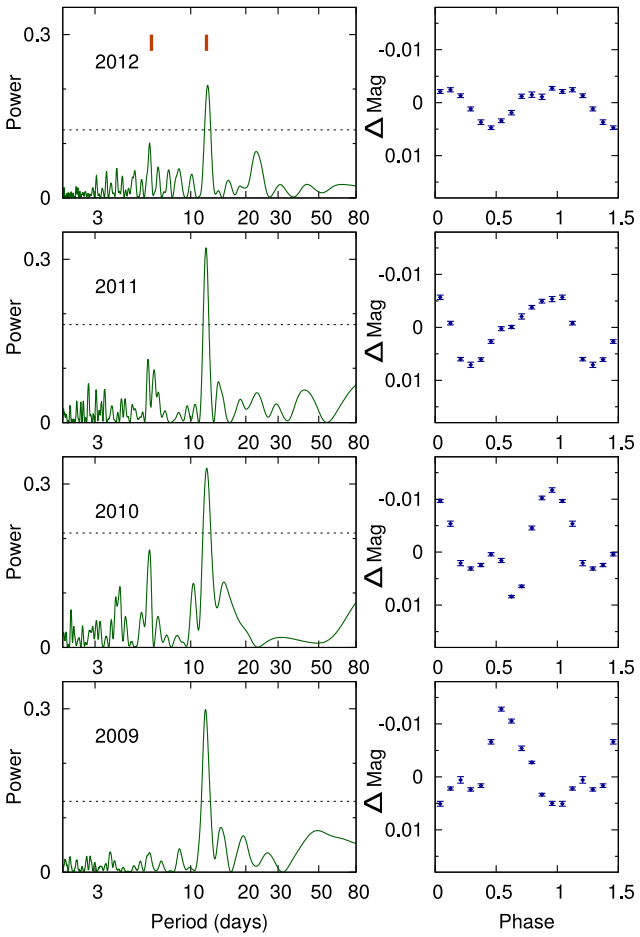

Figure 4. Periodograms of the WASP-South data for HD 73583. The red ticks mark the 12.2-d periodicity and its first harmonic. The dotted line is the estimated 1 per cent-likelihood false-alarm level. The right-hand panels show the data binned and folded on the 12-d period.

observing with a 400–700 nm passband. HD 73583 is 2 mag brighter than any other star in the 48-arcsec photometric aperture. We searched the data for rotational modulations using the methods from Maxted et al. (2011), and found a clear and persistent 12-d periodicity with a false-alarm likelihood below 0.1 per cent. The amplitude ranges from 4 to 7 mmag while the period is 12.2 ± 0.2 d, where the error makes allowance for phase shifts caused by changing star-spot patterns. Fig. 4 shows a visualization of our analysis. We note that this period is consistent with the period of 12.08 ± 0.11 d

recovered in our multidimensional GP analysis (for more details see Section 5.2).

4.4 Stellar age

Given HD 73583 spectral type and well-constrained relatively short rotational period, we expect a relative young age (see Barnes 2003, for more details). We found that the derived age for this star in the literature provides poorly constrained ages (e.g. Delgado Mena et al. 2019, estimated a stellar age of 5.12 ± 4.56 Gyr). We therefore perform some analyses to re-estimate HD 73583's age.

We first use `stardate` (Morton 2015; Angus, Morton & Foreman-Mackey 2019) to infer HD 73583's age using gyrochronology. We input the `SpecMatch-Emp` spectroscopic values, together with the photometry band values and parallax given in Table 1 to `stardate`. For the rotational period of the star, we use the rotational period of the star of 12.08 ± 0.11 d derived in our multidimensional GP analysis of the spectroscopic time-series (see Section 5). We ran 100 000 iterations and we discarded the first 10 000 to create the distributions from which we infer our parameters. `stardate` gives an age of HD 73583 of 750 ± 20 Myr. This analysis puts HD 73583 in the young star regime. However, we note that the error bars come only from the built-in parameter sampling included in `stardate` and they are likely underestimated. We therefore perform additional estimations to provide a more conservative stellar age.

We then use the time–$\log R'_{\rm HK}$ relation of Mamajek & Hillenbrand (2008) to estimate HD 73583's age. With a $\log R'_{\rm HK} = -4.465 \pm 0.015$, HD 73583's is consistent with a star with an age of 480 ± 190 Myr. The error bars include the uncertainties of $\log R'_{\rm HK}$ and the 30 per cent rms on the Mamajek & Hillenbrand (2008)'s fit. In the remainder of this paper, we will assume 480 ± 190 Myr as the stellar age. We note that this stellar age is consistent with the recently reported values by Zhang et al. (2022).

5 EXOPLANET DATA ANALYSIS

5.1 Transit analysis

We first perform a transit analysis in order to obtain planet ephemerides to use for a preliminary RV data analysis in Section 5.2, as well as to check for uniform transit depths in all bands for both planets. We use the code `pyaneti` (Barragán, Gandolfi & Antoniciello 2019; Barragán et al. 2022) to model the flattened *TESS* (see Section 2), *CHEOPS* (see Section 3.2), and ground-base transits (see Section 3.3). To speed up the analysis, we just model data chunks of maximum 3.5 h either side of each transit mid-time.

We sample for the stellar density, $\rho_\star$, and we recover the scaled semimajor axis ($a/R_\star$) for both planets using Kepler's third law (see e.g. Winn 2010). For the limb-darkening model we use the quadratic limb-darkening approach described in Mandel & Agol (2002) with the q_1 and q_2 parametrization given by Kipping (2013). We sample for an independent scaled planet radius ($r_{\rm p} \equiv R_{\rm p}/R_\star$) for each planet in each band. We set uniform priors for all the parameters and we assume circular orbits for both planets. We sample the parameter space with 250 walkers using the Markov chain Monte Carlo (MCMC) ensemble sampler algorithm implemented in `pyaneti` (Foreman-Mackey et al. 2013; Barragán et al. 2019). We created the posterior distributions with the last 5000 iterations of converged chains. We thinned our chains with a factor of 10 giving a distribution of 125 000 independent points for each sampled parameter.

Fig. 5 shows the phase-folded transits for HD 73583 b and c for all the bands they were observed. Fig. 6 shows the posterior distribution for each sampled $r_{\rm p}$ for both planets. We can see that for HD 73583 b, the posteriors for $r_{\rm p}$ for all bands overlap between them, except for the PEST light curve that is consistent with the rest of estimation just within 3σ. The corresponding scaled planet radii are $r_{{\rm p},TESS} = 0.03984^{+0.00079}_{-0.00064}$, $r_{{\rm p},CHEOPS} = 0.03962^{+0.00101}_{-0.00091}$, $r_{\rm p,NGTS} = 0.0404^{+0.0015}_{-0.0015}$, $r_{\rm p,LCO-B} = 0.0394^{+0.0017}_{-0.0019}$, $r_{\rm p,LCO-zs} = 0.0412^{+0.0016}_{-0.0016}$, and $r_{\rm p,PEST} = 0.0494^{+0.0031}_{-0.0032}$. HD 73583 c was only observed with *TESS* and LCO-zs; the scaled planet radii are consistent in these two bands ($r_{{\rm p},TESS} = 0.03325^{+0.00075}_{-0.00073}$, and $r_{\rm p,LCO-zs} = 0.0344^{+0.0023}_{-0.0025}$, see also the posteriors in Fig. 6). We also note that the recovered stellar density from this analysis is $3.05^{+0.51}_{-0.69}$ g cm^{-3}, consistent with the value obtained in the stellar analysis presented in Section 4.2.

We then repeated the analysis, but this time sampling for a single $r_{\rm p,\,full}$ for each planet, i.e. assuming that, for a given planet, all the transits have the same depth in all bands. Fig. 6 shows the posterior distribution obtained in this analysis for HD 73583 b and c. We can see that for HD 73583 b the combination of all transits in all bands provides a better constrain on the scaled planetary radius of $r_{\rm p,full} = 0.0399^{+0.00064}_{-0.00054}$. This shows the advantages of performing space- and ground-base transit follow-up of *TESS* planets to improve the measurement of planetary radii. For HD 73583 c we can see that the posterior of $r_{\rm p,\,full}$ is practically identical to the posterior of $r_{{\rm p},TESS}$, which is expected given that the ground-base observations of HD 73583 c observed only partial transits.

We also note that all transit data improve the constrain on the ephemerides that have a direct impact to plan future follow-up observations. We obtain a time of mid-transit and orbital period of 1517.69016 ± 0.00063 BTJD and 6.3980422 ± 0.0000070 d for HD 73583 b, and 1232.1682 ± 0.0025 BTJD and 18.87981 ± 0.00090 d for HD 73583 c, respectively. We use these values to perform our spectroscopic time-series modelling in Section 5.2. In Section 5.3, we perform a joint analysis with transits and spectroscopic time-series.

5.2 Multidimensional GP approach

We perform a multidimensional GP (hereafter multi-GP) approach to characterize the stellar and planetary signals in our RV time-series (see Rajpaul et al. 2015, for more details). We create a two-dimensional GP model described as

$$\begin{aligned} RV &= A_{\rm RV} G(t) + B_{\rm RV} \dot{G}(t), \\ S_{\rm HK} &= A_{\rm S} G(t), \end{aligned} \tag{1}$$

where $G(t)$ is a latent (unobserved) variable, which can be loosely interpreted as representing the projected area of the visible stellar disc that is covered in active regions at a given time. The amplitudes $A_{\rm RV}$, $B_{\rm RV}$, and $A_{\rm S}$ are free parameters which relate the individual time-series with $G(t)$. To constrain the stellar signal in our data we use $S_{\rm HK}$ that has been proven to be a good tracer of the area covered for active regions on the stellar surface (see e.g. Isaacson & Fischer 2010; Thompson et al. 2017). It is also worth to mention that the Ca II H and K activity indicators ($S_{\rm HK}$ and $\log R'_{\rm HK}$) have been proved to constrain the $G(t)$ function for active G and K-type stars in previous multi-GP analyses (e.g. Barragán et al. 2019; Georgieva et al. 2021).

We perform a multi-GP regression on the HARPS, HIRES, PFS, and CORALIE RV and $S_{\rm HK}$ time-series. We created our covariance

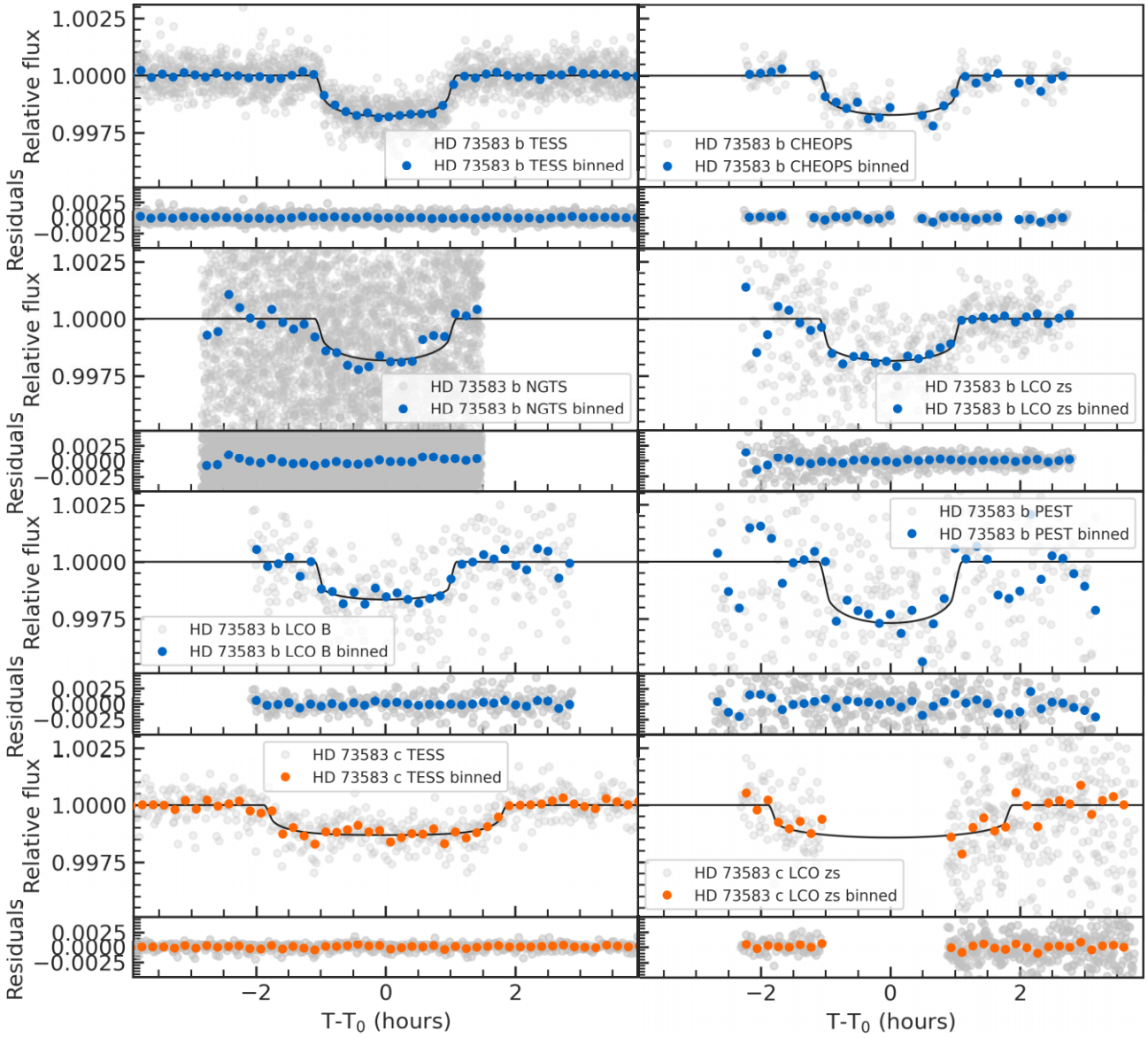

Figure 5. Phase-folded light curves of HD 73583 b (panels with blue circles) and HD 73583 c (panels with orange circles) for different bands. Nominal observations are shown in light grey. Solid colour circles represent 10-min binned data. Transit models are shown with a solid black line.

matrix using the Quasi-Periodic kernel

$$\gamma(t_i, t_j) = \exp\left[-\frac{\sin^2[\pi(t_i - t_j)/P_{\rm GP}]}{2\lambda_{\rm P}^2} - \frac{(t_i - t_j)^2}{2\lambda_{\rm e}^2}\right], \quad (2)$$

and its derivatives (see Rajpaul et al. 2015; Barragán et al. 2022, for more details). In equation (2) $P_{\rm GP}$ is the GP characteristic period, $\lambda_{\rm p}$ the inverse of the harmonic complexity, and $\lambda_{\rm e}$ is the long-term evolution time-scale.

We performed a multi-GP regression using `pyaneti` (as described in Barragán et al. 2022). We created our RV residual vector by modelling an offset for each spectrograph and two Keplerian signals with the ephemeris given in our transit analysis and assuming circular orbits. For the $S_{\rm HK}$ time-series we account for a different offset for each instrument. We note that we are using four different spectrographs that observe in similar wavelength ranges and we expect the spot contrast to be similar. For this reason we consider that there is no chromatic variation between them and we assume that the stellar activity can be described with the same underlying function for all four instruments.

We perform an MCMC analysis using Gaussian priors on the planet ephemerides given in Section 5.1. For the remainder sampled parameters we use uniform priors. We note that we did not train our GP hyper-parameters using the *TESS* or WASP-South light curves (see Haywood et al. 2014, for more details on training GPs for RV modelling). The active regions on the stellar surface may be different and therefore the stellar signal may be described with a GP with a different set of hyper-parameters (see e.g. Barragán et al. 2021). We therefore use uniform priors to sample for the multi-GP hyper-parameters (we chose an uniform prior around 12 d for the period based on the analyses presented in Section 4.3). We sample the parameter space with 250 independent Markov chains and we use the last 5000 converged chains and a thin factor of 10 to create posterior distributions with 125 000 independent samples for each parameter. We obtained unimodal posterior distributions for all the sampled parameters. This analysis provides a detection of

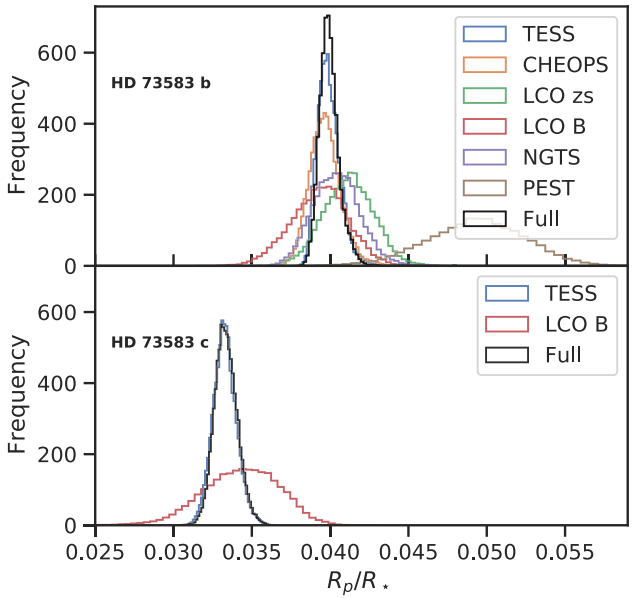

Figure 6. Posterior distributions for the multiradius (colourful posteriors) and single-radius (black posteriors) transit modellings, for planet b (top panel) and c (bottom panel). Both panels are shown with the same x- and y-scale to facilitate comparison.

two Keplerian signals that match the transiting exoplanet ephemeris. HD 73583 b and c induce a Doppler wobble with semi-amplitudes of $4.3^{+1.43}_{-1.15}$ m s^{-1}and $2.74^{+0.57}_{-0.56}$ m s^{-1} on its host star, respectively. In Section 6.1, we make a further discussion on the inferred stellar and planetary signals.

It is worth to note that the precision of the recovered Doppler signal of HD 73583 c is better than for HD 73583 b. This is a consequence of the orbital period of HD 73583 b (∼6.4 d) being close to the first harmonic of the rotational period of the star (∼6 d). This imperils the precision with which HD 73583 b Keplerian signal can be recovered.

5.3 Joint analysis

Following our analyses described in Sections 5.1 and 5.2, we proceed to perform a final analysis combining our transit and spectroscopic time-series modelling. This analysis combines the same assumptions described in Sections 5.1 and 5.2 with a few differences. Now we allow for eccentric orbits for both planetary orbits; we set a Gaussian prior on the stellar density based on our results in Section 4, and we fit for a common scaled planet radius for all the bands for each planet. All sampled parameters and priors used for this analysis can be found in Table 4. We note that 14 of the sampled parameters are jitter terms per instrument that we added in our likelihood to penalize for imperfections in our model (see Barragán et al. 2022). We sample the parameter space with 500 independent Markov chains. We create posterior distributions with 250 000 sampled points for each parameter using the last 25 000 converged chains and a thin factor of 50. Given the high dimensionality of the parameter space (55 parameters), we ran this set-up 10 times. We found that the code arrives to consistent parameter solutions in every independent run. This give us confidence that the derived parameters are reliable.

Table 4 shows the inferred values for all the sampled parameters. They are given as the median and 68.3 per cent region of the credible interval from the posterior distribution of each parameter. In Fig. A1, we show the posterior and correlation plots for some of the sampled parameter. Table 5 shows the derived planetary, orbital, and stellar parameters. HD 73583 b and c are detected in the RV time-series with Doppler semi-amplitudes of $4.37^{+1.46}_{-1.31}$ and $2.89^{+0.53}_{-0.51}$ m s^{-1}, respectively. Fig. 7 shows the RV and $S_{\rm HK}$ time-series together with the inferred models. Fig. 8 shows the phase-folded RV curve for each planetary induced signal.

6 DISCUSSION AND CONCLUSIONS

6.1 Stellar signal characterization

The GP hyper-parameters are well constrained with the values $P_{\rm GP}$= $12.024^{+0.095}_{-0.087}$ d, $\lambda_{\rm e}$= 32^{+7}_{-6} d, and $\lambda_{\rm p}$= $0.432^{+0.050}_{-0.046}$. We can argue that $P_{\rm GP}$ describes the star's rotation period, given that is in agreement with the results obtained with WASP-South photometry (Section 4.3). The recovered $\lambda_{\rm e}$ is significantly larger than the recovered $P_{\rm GP}$. This suggests that the same active regions on the stellar surface are present for almost three stellar rotations. This also indicates that the QP kernel is a good choice to describe the scales of the stellar signal in our data (see Rajpaul et al. 2015, for a discussion on this). Finally, the recovered $\lambda_{\rm p}$ implies a relatively high harmonic complexity for the underlying process describing the stellar signal. This suggests that there are diverse groups of active regions on the stellar surface, leading to complex patterns in our spectroscopic time-series.

Fig. 7 shows the inferred model for the stellar signal in the RV and $S_{\rm HK}$ time-series. Such curves are consistent with a high harmonic complexity scenario having several 'beat' patterns within each period. However, the process describing the RV stellar signal has an apparent higher harmonic complexity than the $S_{\rm HK}$ one. This can be explained by the sensitivity of RV activity induced signals to the position and motion of the active regions on the visible stellar disc, creating complex patterns (see e.g. Dumusque, Boisse & Santos 2014). Fortunately, this complexity can be described, as a first order approach, as the derivative of the function $G(t)$ that describes the area covered by active regions on the stellar surface as a function of time (Aigrain, Pont & Zucker 2012; Rajpaul et al. 2015). This can be seen empirically in this system as the recovered amplitudes for the GP describing the RV time-series are $A_{\rm RV} = 0.53^{+0.46}_{-0.33}$ m s^{-1} (with a posterior truncated at zero, see Fig. A1) and $B_{\rm RV} = 17.3^{+3.1}_{-2.6}$ m s^{-1} d, i.e a significant detection (see Fig. A1). We can also see that the process describing the stellar signal in the $S_{\rm HK}$ time-series has an amplitude of $0.022^{+0.0041}_{-0.0034}$ that is significantly different from zero. This suggest that the stellar signal in the $S_{\rm HK}$ is also constrained with our model (for more discussion on this see Appendix C2). This demonstrates that for HD 73583, the RV signal is mainly described by $\dot{G}(t)$, while $S_{\rm HK}$ time-series is well described by $G(t)$. We note that this behaviour has been observed empirically in other young stars that show high harmonic complexity (e.g, Barragán et al. 2019). For a further discussion on the importance of the derivative of the GPs when dealing with high harmonic complexity, see Barragán et al. (2022). In Appendix C, we show further tests that we perform in order to ensure that our stellar modelling is robust.

As we mention in Section 5.2, we assume there is no chromatic variation of the stellar signal between our four different spectrographs. From Fig. 7 we can see that PFS and HIRES data overlap with some HARPS observations. Fig. 7 shows that the PFS and HIRES observations are consistent with the same time-scales and amplitudes as the HARPS data set. This encourages that our assumption of describing different instruments that observe in similar wavelengths with the same underlying function is correct. We note that the CORALIE observations were taken months before the rest of our

Table 4. Model parameters and priors for joint fit.

Parameter	Prior[a]	Final value[b]
HD 73583 b's parameters		
Orbital period $P_{\rm orb}$ (d)	$\mathcal{U}[6.3973, 6.3982]$	$6.3980420^{+0.0000067}_{-0.0000062}$
Transit epoch T_0 ($\rm BJD_{TDB}$ −2450000)	$\mathcal{U}[8517.5460, 8517.8040]$	$8517.69013^{+0.00056}_{-0.00059}$
Scaled planet radius $R_{\rm p}/R_\star$	$\mathcal{U}[0.0, 0.05]$	$0.03932^{+0.00066}_{-0.00061}$
Impact parameter, b	$\mathcal{U}[0, 1]$	$0.566^{+0.070}_{-0.068}$
$\sqrt{e}\sin\omega_\star$	$\mathcal{U}[-1, 1]$	$-0.03^{+0.17}_{-0.18}$
$\sqrt{e}\cos\omega_\star$	$\mathcal{U}[-1, 1]$	$-0.22^{+0.24}_{-0.15}$
Doppler semi-amplitude variation K ($\rm m\,s^{-1}$)	$\mathcal{U}[0, 50]$	$4.37^{+1.46}_{-1.31}$
HD 73583 c's parameters		
Orbital period $P_{\rm orb}$ (d)	$\mathcal{U}[18.78, 18.98]$	$18.87974^{+0.00086}_{-0.00074}$
Transit epoch T_0 ($\rm BJD_{TDB}$ −2450000)	$\mathcal{U}[9232.06, 9232.26]$	$9232.1682^{+0.0019}_{-0.0024}$
Scaled planet radius $R_{\rm p}/R_\star$	$\mathcal{U}[0.0, 0.05]$	$0.03368^{+0.00089}_{-0.00083}$
Impact parameter, b	$\mathcal{U}[0, 1]$	$0.21^{+0.23}_{-0.15}$
$\sqrt{e}\sin\omega_\star$	$\mathcal{U}[-1, 1]$	$-0.15^{+0.18}_{-0.17}$
$\sqrt{e}\cos\omega_\star$	$\mathcal{U}[-1, 1]$	$0.16^{+0.17}_{-0.21}$
Doppler semi-amplitude variation K ($\rm m\,s^{-1}$)	$\mathcal{U}[0, 50]$	$2.89^{+0.53}_{-0.51}$
GP hyper-parameters		
GP period $P_{\rm GP}$ (d)	$\mathcal{U}[10, 14]$	12.08 ± 0.11
$\lambda_{\rm p}$	$\mathcal{U}[0.1, 5]$	$0.467^{+0.042}_{-0.038}$
$\lambda_{\rm e}$ (d)	$\mathcal{U}[1, 500]$	$27.28^{+7.26}_{-4.35}$
$A_{\rm RV}$ ($\rm m\,s^{-1}$)	$\mathcal{U}[0, 100]$	$0.53^{+0.46}_{-0.33}$
$B_{\rm RV}$ ($\rm m\,s^{-1}$ d)	$\mathcal{U}[-1000, 1000]$	$17.3^{+3.1}_{-2.6}$
$A_{\rm S}$	$\mathcal{U}[0, 1]$	$0.022^{+0.0041}_{-0.0034}$
Other parameters		
Stellar density $\rho_\star$ ($\rm g\,cm^{-3}$)	$\mathcal{N}[3.48,0.35]$	3.69 ± 0.35
TESS Parametrized limb-darkening coefficient q_1	$\mathcal{U}[0, 1]$	$0.35^{+0.23}_{-0.16}$
TESS Parametrized limb-darkening coefficient q_2	$\mathcal{U}[0, 1]$	$0.16^{+0.27}_{-0.12}$
CHEOPS Parametrized limb-darkening coefficient q_1	$\mathcal{U}[0, 1]$	$0.29^{+0.17}_{-0.12}$
CHEOPS Parametrized limb-darkening coefficient q_2	$\mathcal{U}[0, 1]$	$0.47^{+0.31}_{-0.30}$
NGTS Parametrized limb-darkening coefficient q_1	$\mathcal{U}[0, 1]$	$0.64^{+0.24}_{-0.28}$
NGTS Parametrized limb-darkening coefficient q_2	$\mathcal{U}[0, 1]$	$0.37^{+0.22}_{-0.23}$
LCO-zs Parametrized limb-darkening coefficient q_1	$\mathcal{U}[0, 1]$	$0.33^{+0.32}_{-0.2}$
LCO-zs Parametrized limb-darkening coefficient q_2	$\mathcal{U}[0, 1]$	$0.37^{+0.33}_{-0.26}$
LCO-B Parametrized limb-darkening coefficient q_1	$\mathcal{U}[0, 1]$	$0.23^{+0.31}_{-0.17}$
LCO-B Parametrized limb-darkening coefficient q_2	$\mathcal{U}[0, 1]$	$0.33^{+0.36}_{-0.24}$
PEST Parametrized limb-darkening coefficient q_1	$\mathcal{U}[0, 1]$	$0.51^{+0.34}_{-0.32}$
PEST Parametrized limb-darkening coefficient q_2	$\mathcal{U}[0, 1]$	$0.31^{+0.26}_{-0.22}$
Offset HARPS RV ($\rm km\,s^{-1}$)	$\mathcal{U}[20.2311, 21.2728]$	$20.75208^{+0.00043}_{-0.00043}$
Offset PFS RV ($\rm km\,s^{-1}$)	$\mathcal{U}[-0.5253, 0.5219]$	$-0.00319^{+0.0008}_{-0.00093}$
Offset HIRES RV ($\rm km\,s^{-1}$)	$\mathcal{U}[-0.5253, 0.5219]$	$0.0066^{+0.0021}_{-0.0023}$
Offset CORALIE RV ($\rm km\,s^{-1}$)	$\mathcal{U}[20.2129, 21.2589]$	$20.7371^{+0.0029}_{-0.0029}$
Offset HARPS $S_{\rm HK}$	$\mathcal{U}[0.3141, 1.4507]$	$0.8793^{+0.0076}_{-0.0073}$
Offset PFS $S_{\rm HK}$	$\mathcal{U}[-0.0856, 1.0419]$	$0.4491^{+0.0099}_{-0.0098}$
Offset HIRES $S_{\rm HK}$	$\mathcal{U}[0.1008, 1.1666]$	$0.6369^{+0.0093}_{-0.0096}$
Offset CORALIE $S_{\rm HK}$	$\mathcal{U}[0.1956, 1.2995]$	$0.7265^{+0.0097}_{-0.0099}$
Jitter term $\sigma_{\rm RV,\,HARPS}$ ($\rm m\,s^{-1}$)	$\mathcal{J}[1, 100]$	$2.05^{+0.59}_{-0.51}$
Jitter term $\sigma_{\rm RV,\,PFS}$ ($\rm m\,s^{-1}$)	$\mathcal{J}[1, 100]$	$1.87^{+0.64}_{-0.44}$
Jitter term $\sigma_{\rm RV,\,HIRES}$ ($\rm m\,s^{-1}$)	$\mathcal{J}[1, 100]$	$5.84^{+3.04}_{-1.59}$
Jitter term $\sigma_{\rm RV,\,CORALIE}$ ($\rm m\,s^{-1}$)	$\mathcal{J}[1, 100]$	$2.62^{+4.65}_{-2.1}$

Table 4 – *continued*

Parameter	Prior[a]	Final value[b]
Jitter term $\sigma_{S_{HK},HARPS}(\times 10^3)$	$\mathcal{J}[1, 100]$	$17.15^{+1.91}_{-1.66}$
Jitter term $\sigma_{S_{HK},PFS}(\times 10^3)$	$\mathcal{J}[1, 100]$	$28.31^{+5.26}_{-4.15}$
Jitter term $\sigma_{S_{HK},HIRES}(\times 10^3)$	$\mathcal{J}[1, 100]$	$5.84^{+3.04}_{-1.59}$
Jitter term $\sigma_{S_{HK},CORALIE}(\times 10^3)$	$\mathcal{J}[1, 100]$	$20.95^{+9.71}_{-10.84}$
TESS jitter term σ_{TESS} ($\times 10^{-6}$)	$\mathcal{J}[0, 1 \times 10^3]$	$0.0006782^{+7.9e-06}_{-7.8e-06}$
CHEOPS jitter term σ_{CHEOPS} ($\times 10^{-6}$)	$\mathcal{J}[0, 1 \times 10^3]$	$0.00045^{+2.8e-05}_{-2.6e-05}$
NGTS jitter term σ_{NGTS} ($\times 10^{-6}$)	$\mathcal{J}[0, 1 \times 10^3]$	$0.0037^{+6.7e-05}_{-7e-05}$
LCO-zs jitter term σ_{LCO-zs} ($\times 10^{-6}$)	$\mathcal{J}[0, 1 \times 10^3]$	$0.001665^{+4.4e-05}_{-4e-05}$
LCO-B jitter term σ_{LCO-B} ($\times 10^{-6}$)	$\mathcal{J}[0, 1 \times 10^3]$	$0.00126^{+7.2e-05}_{-6.9e-05}$
PEST jitter term σ_{PEST} ($\times 10^{-6}$)	$\mathcal{J}[0, 1 \times 10^3]$	$0.00338^{+0.00014}_{-0.00014}$

Notes.[a]$\mathcal{U}[a, b]$ refers to uniform priors between a and b, $\mathcal{N}[a, b]$ to Gaussian priors with mean a and standard deviation b, and $\mathcal{J}[a, b]$ to the modified Jeffrey's prior as defined by Gregory (2005, eq. 16).
[b]Inferred parameters and errors are defined as the median and 68.3 per cent credible interval of the posterior distribution.

Table 5. Derived parameters for the HD 73583 planets.

Parameter	HD 73583 b's values	HD 73583 c's values
Planet mass M_p ($M_\oplus$)	$10.2^{+3.4}_{-3.1}$	$9.7^{+1.8}_{-1.7}$
Planet radius R_p ($R_\oplus$)	2.79 ± 0.10	$2.39^{+0.10}_{-0.09}$
Planet density ρ_p (g cm^{-3})	$2.58^{+0.95}_{-0.81}$	$3.88^{+0.91}_{-0.80}$
Scaled semimajor axis $a/R_\star$	$19.98^{+0.61}_{-0.63}$	$41.11^{+1.25}_{-1.3}$
Semimajor axis a (AU)	$0.0604^{+0.0027}_{-0.0026}$	$0.1242^{+0.0055}_{-0.0054}$
Eccentricity e	$0.09^{+0.09}_{-0.06}$	$0.08^{+0.11}_{-0.06}$
angle of periastron $\omega_\star$	-76^{+234}_{-86}	$-41.6^{+52.8}_{-47.7}$
Orbit inclination i_p (°)	88.37 ± 0.18	$89.72^{+0.20}_{-0.27}$
Transit duration τ_{14} (h)	$2.143^{+0.029}_{-0.027}$	$3.67^{+0.09}_{-0.102}$
RV at mid-transit time (km s^{-1})	$6.3^{+9.6}_{-6.5}$	$-3.1^{+3.7}_{-6.3}$
Planet surface gravity g_p (cm s^{-2})[(a)]	1268^{+448}_{-389}	1632^{+338}_{-310}
Planet surface gravity g_p (cm s^{-2})[(b)]	1288^{+453}_{-395}	1658^{+344}_{-317}
Equilibrium temperature T_{eq} (K)[(c)]	714^{+21}_{-20}	498 ± 15
Received irradiance ($F_\oplus$)	$43.3^{+5.3}_{-4.7}$	$10.2^{+1.2}_{-1.1}$
TSM[(d)]	136^{+60}_{-35}	62^{+15}_{-11}

Notes.[a]Derived using $g_p = G M_p R_p^{-2}$.
[b]Derived using sampled parameters following Southworth et al. (2007).
[c]Assuming a zero albedo.
[d]Transmission spectroscopy metric (TSM) by Kempton et al. (2018).

RV data, and given the $\lambda_e = 27.28^{+7.26}_{-4.35}$ d, we expect that HD 73583 had a different configuration of active regions at that time. However, we note that the CORALIE observations seem to have the same amplitudes and scales as the RVs of the other instruments.

6.2 Dynamical analysis

We performed an orbital stability analysis of the HD 73583 system using the software `mercury6` (Chambers 1999). We assume that both planets have coplanar orbits and we use our derived parameters in Table 5 to create our `mercury6` set-up. We evolved the system for 1 Gyr with steps of 0.5 d per integration. For HD 73583 b we found negligible changes on the orbital parameters of the planet, except for the eccentricity that fluctuated with a maximum change of 0.08. For HD 73583 c we found changes of its eccentricity <0.08 and a maximum variation of 5×10^{-5} AU in its semimajor axis. Therefore, we conclude that the orbital and planetary parameters derived for HD 73583 are consistent with a dynamically stable system.

6.3 Exoplanet compositions

Fig. 9 shows a mass–radius diagram for small exoplanets ($1 < R_p < 4\,R_\oplus$ and $1 < M_p < 20 M_\oplus$) detected with a precision better than 30 per cent in radius and mass. We also overplot the two layer exoplanet models by Zeng, Sasselov & Jacobsen (2016), together with the Earth-like interior plus Hydrogen envelope models given by Zeng et al. (2019). With a mass of $10.2^{+3.4}_{-3.1}\ M_\oplus$ and radius of $2.79 \pm 0.10\ R_\oplus$, HD 73583 b has a density of $2.58^{+0.95}_{-0.81}$ g cm^{-3}. HD 73583 b lies above the pure water composition model. This implies that some percentage of the planet radius has to be gaseous (see e.g. Russell 2021). With an equilibrium temperature of 714^{+21}_{-20} K HD 73583 b is consistent with a composition made of an Earth-like interior with a thick Hydrogen envelope accounting for approximately 2 per cent of the planet's mass. None the less, we note that there is a degeneracy on determining exoplanet compositions in a mass–radius diagram. For example, it is also possible to explain HD 73583 b with a water-rich interior with an Hydrogen envelope that accounts for only 0.3 per cent of the planet's mass (we do not show such models in Fig. 9, for more details see Zeng et al. 2019). The other planet, HD 73583 c, has a mass of $9.7^{+1.8}_{-1.7}\ M_\oplus$ similar to HD 73583 b but a significantly smaller radius of $2.39^{+0.10}_{-0.09}\ R_\oplus$. This gives a bulk density of $3.88^{+0.91}_{-0.80}$ g cm^{-3} for HD 73583 c, which puts it below the pure water composition model. Therefore, HD 73583 c is consistent with a solid water-rich world made of 50 per cent water ice and 50 per cent silicates. However, we can see that HD 73583 c is also consistent with a planet made of a Earth-like interior, surrounded by a Hydrogen envelope that could account for 1 per cent of its mass (taking into account its equilibrium temperature of 498 ± 15 K).

Fig. 10 shows an insolation versus planetary radius diagram with the approximate positions of the Neptunian desert and radius valley indicated with text. It is worth to note that HD 73583 b and c lie well above the radius valley. We therefore expect that both planets have a volatile envelope rather than being solid worlds, as suggested by previous works (Fulton et al. 2017; Van Eylen et al. 2018). Despite

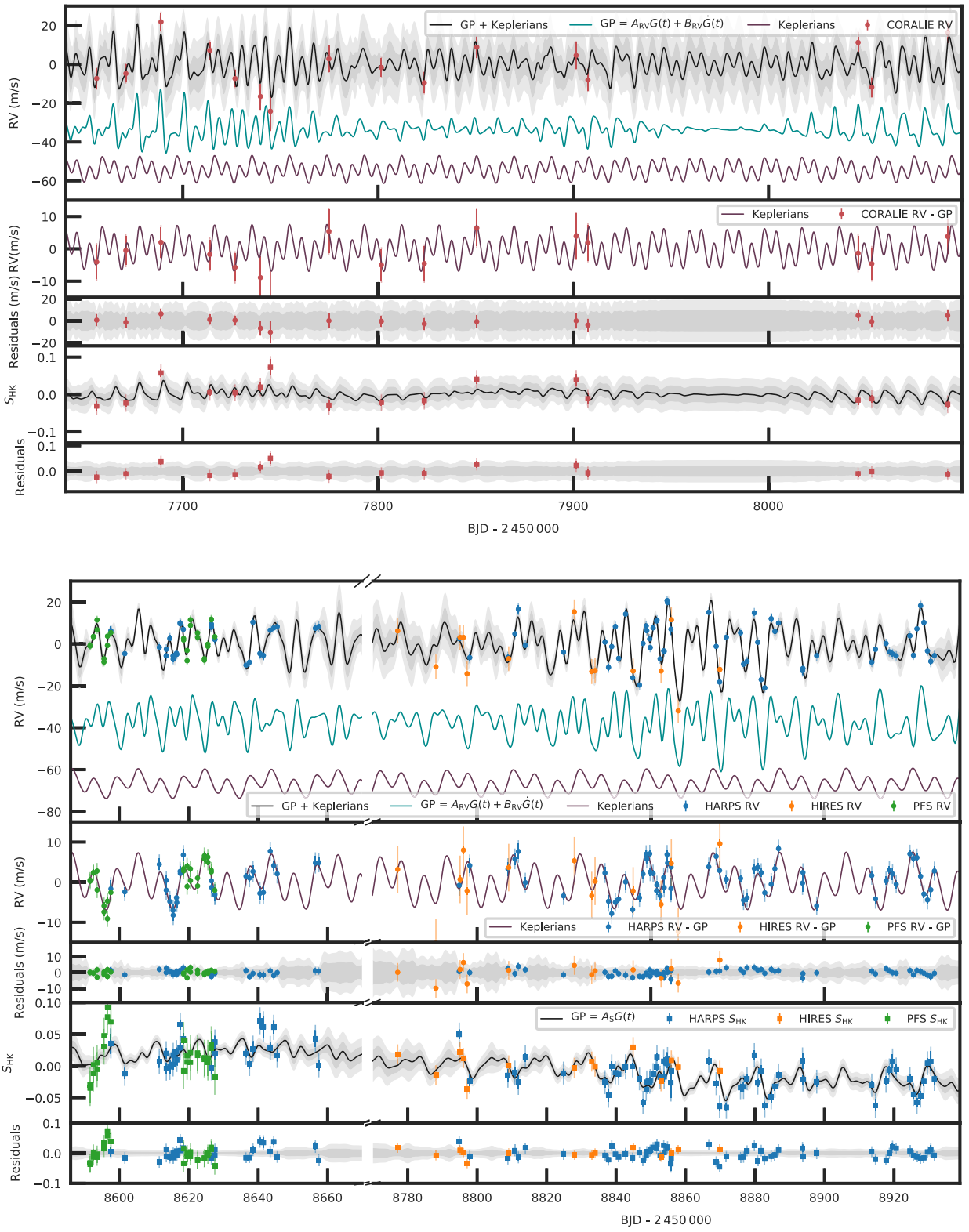

Figure 7. RV and S_{HK} time-series after been corrected by inferred offsets. Each plot shows (from top to bottom): RV data together with full, stellar, and planetary signal inferred models; RV data with stellar signal model subtracted; RV residuals; S_{HK} data together with inferred stellar model, and S_{HK} residuals. The upper plot shows CORALIE (red) observations. The bottom plot displays HARPS (blue), HIRES (orange), and PFS (green) data. Measurements are shown with filled symbols with error bars with a semitransparent error bar extension accounting for the inferred jitter. The solid (black) lines show the inferred full model coming from our multi-GP, light grey shaded areas showing the 1σ and 2σ credible intervals of the corresponding GP model. For the RV time-series we also show the inferred stellar (cyan line) and planetary (dark purple line) recovered signals with an offset for better clarity. We note that in the bottom plot there is a gap between 8670 and 8770 BJD – 2450000 where there were no measurements.

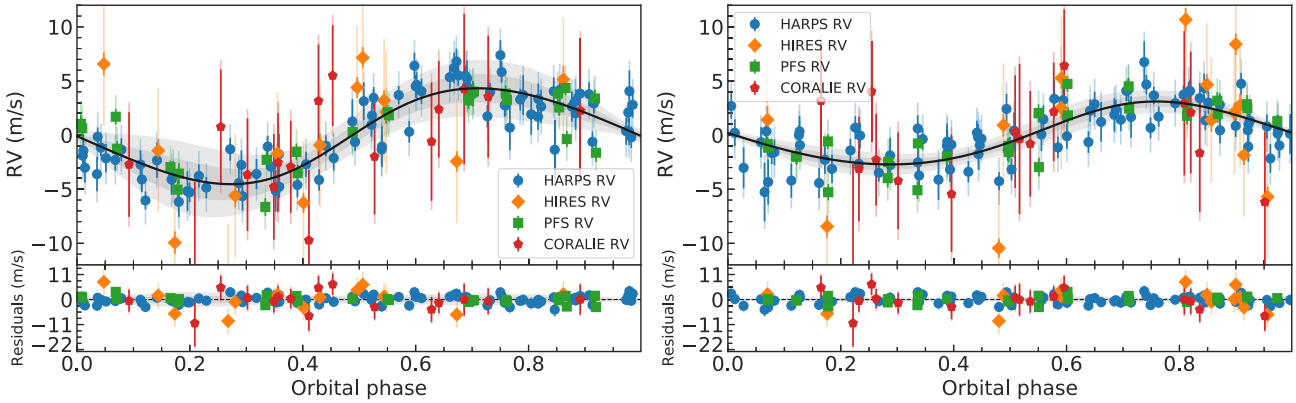

Figure 8. Phase-folded RV signals for HD 73583 b (left) and HD 73583 c (right) following the subtraction of the systemic velocities, stellar signal, and other planets. HARPS (blue circles), HIRES (orange diamonds), PFS (green squares), and CORALIE (red pentagons) RV observations are shown. RV models are shown (solid black line) with 1σ and 2σ credible intervals (shaded areas). In all the plots the nominal error bars are in solid colour, and the error bars taking into account the jitter are semitransparent.

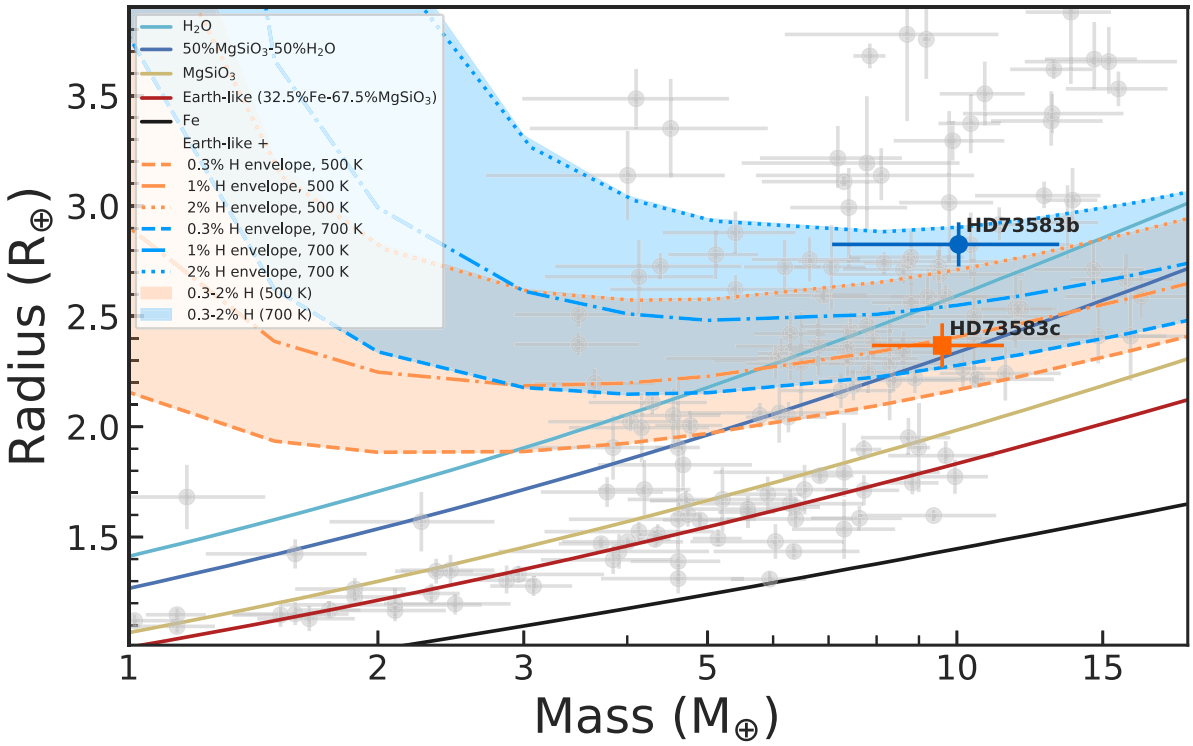

Figure 9. Mass *versus* radius diagram for small exoplanets ($1 < R_p < 4\,R_\oplus$ and $1 < M_p < 20\,M_\oplus$). The grey points with error bars show planets with mass and radius measurements better than 30 per cent (As in the TEPCAT catalogue, https://www.astro.keele.ac.uk/jkt/tepcat/, Southworth et al. 2007). HD 73583 b and c are shown with a (blue) circle and a (orange) square, respectively. The solid lines represent two-layer models as given by Zeng et al. (2016) with a different colour corresponding to a different mixture of elements. The non-solid lines correspond to rocky cores surrounded by an Hydrogen envelope with 0.3 per cent (dashed line), 1 per cent (dash-dotted line), and 2 per cent (dotted line) Hydrogen mass for exoplanets with equilibrium temperatures of 500 K (orange, similar to HD 73583 c's T_{eq}) and 700 K (blue, similar HD 73583 b's T_{eq}) as given by Zeng et al. (2019).

the degeneracy in composition for both planets, for the remainder of the discussion in this manuscript we will assume that HD 73583 b and c have an Earth-like interior surrounded by a Hydrogen-rich volatile envelope. A discussion of the planetary characteristics assuming different composition scenarios is out of the scope of this paper.

We note that HD 73583 b has a lower density than HD 73583 c, but they both have similar masses. According to Zeng et al. (2019), planets with the same mass and same volatile Hydrogen content would have different radii (hence different density) if their temperatures are significantly different, being a hotter planet more bloated due to thermal inflation. We note that HD 73583 b is ~200 K hotter than HD 73583 c and we would then expect a larger radius for it. However, the difference in temperature between HD 73583 b and c is not enough to explain the $\sim 0.5 R_\oplus$ difference in radii between both planets. The difference in radii can be explained by extra Hydrogen content in the atmosphere of HD 73583 b, with respect to HD 73583 c (see Fig. 9). This is unexpected if we assume that this system has

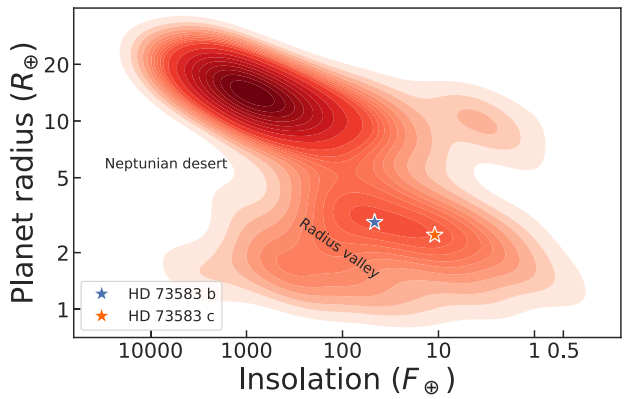

Figure 10. Insolation versus planetary radius diagram. The red contours show the occurrence of transiting exoplanets (As in the TEPCAT catalogue). HD 73583 b and HD 73583 c are represented with a blue and orange star, respectively. The approximately locations of the 'hot Neptunian desert' and 'radius valley' are shown for guidance.

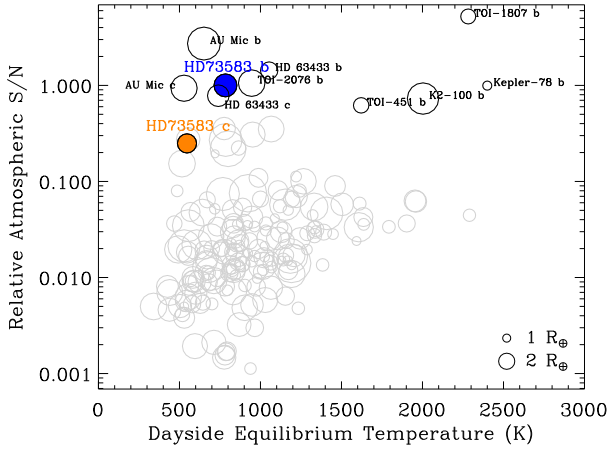

Figure 11. Relative S/N of an atmospheric signal for all young (<1 Gyr) exoplanet candidates with $R_p < 5R_\oplus$. Circle's size shows the planetary radius. HD 73583 b and HD 73583 c are shown with a filled blue and orange circles, respectively. HD 73583 b is used as the S/N reference.

been shaped by photoevaporation, in which the innermost planet is expected to have a more depleted atmosphere (e.g. Owen & Wu 2013; Lopez & Fortney 2014). In Fig. 10, we can see that both planets lie far from the high irradiated hot Neptunian desert and the radius valley regions. This suggests that the photoevaporation process may be slow. In this low irradiation regime, core-powered mass-loss mechanisms could also play an important role sculpting the planet's atmospheres (Gupta & Schlichting 2021). Given their youth, both planets could still evolve and experience atmospheric mass-loss.

6.4 Atmospheric characterization perspectives

6.4.1 Transmission spectroscopy generalities

We emphasize that from now on our analyses and conclusions assume that HD 73583 b and c are Earth-like interior + H/He envelope planets. Because of their youth, extended atmosphere, and host star brightness, HD 73583 b and c are excellent candidates to perform transmission spectroscopy. We note that HD 73583 b has a Transmission spectroscopic metric (TSM) of 136^{+60}_{-35} , which is well above the threshold at 90 suggested by Kempton et al. (2018). Therefore, this target is highly valuable target for the *James Webb Space Telescope* (*JWST*). We note that HD 73583 c's TSM value of 62^{+15}_{-11} is below the threshold. However, we discuss here the atmospheric study perspectives for both planets.

Fig. 11 displays a relative atmospheric detection S/N metric (normalized to HD 73583 b) for all well-characterized young transiting planets with $R < 5\ R_\oplus$. The sample is taken from the NASA Exoplanet Archive. The atmospheric signal is calculated in a similar way in Niraula et al. (2017). The atmospheric signal is dominated by the atmospheric scale height, favouring hot, extended atmospheres, and the host star radius, favouring small, cool stars. The relative S/N calculation scales with properties that make it favourable to detect and measure this signal. Our metric is similar to the TSM in Kempton et al. (2018). The difference with our metric is that instead of calculating this per transit, we calculate it based on time, thus adding a $P^{-0.5}$ term. Given the observational challenges of observing planets in transit with highly oversubscribed facilities, the frequency of transits is a very important constraint on obtaining atmospheric measurements. We assume an effective scale height ($h_{\rm eff}$ = 7 Hill radii; Miller-Ricci, Seager & Sasselov 2009) using the equilibrium temperature, a Bond albedo of $\alpha = 0.3$, and an atmospheric mean molecular weight of $\mu = 20$. Because this is a relative assessment, and we are assuming identical properties for all the atmospheres in this sample, the precise value of these variables do not change the results. Table 6 shows the top 10 best young planets candidates in terms of expected S/N. HD 73583 b occupies the fifth position in this rank, making it an excellent target for transmission spectroscopy follow-up efforts. Even if not showed in Table 6, we note that HD 73583 c lies in the 16th position in the same ranking. It is worth to mention that the scientific value of HD 73583 b and c is even higher given that both planets form part of the same system. This will allow to perform comparative atmospheric composition and mass-loss studies that are crucial to test theoretical models.

Table 6. Top 10 best young exoplanets candidates for transmission spectroscopy S/N normalized to HD 73583 b, which is highlighted in bold.

Rank	Name	$T_{\rm eq}$ atmosphere	S/N relative to HD 73583 b	$R_\star$	Orbital period
1	TOI-1807 b	2282.4	5.217	0.68	0.5494
2	AU Mic b	651.2	2.725	0.75	8.4630
3	HD 63433 b	1053.7	1.425	0.91	7.1079
4	TOI-2076 b	945.9	1.056	0.76	10.3557
5	**HD 73583 b**	**783.9**	**1.000**	**0.66**	**6.3980**
6	Kepler-78 b	2400.0	0.994	0.75	0.3550
7	AU Mic c	528.5	0.934	0.75	18.8590
8	HD 63433 c	739.8	0.781	0.91	20.5453
9	K2-100 b	2003.3	0.729	1.24	1.6739
10	TOI-451 b	1621.6	0.620	0.88	1.8587

6.4.2 Hydrogen escape

Using the 1D hydrodynamic escape model described in Allan & Vidotto (2019), we predict the planetary upper atmosphere properties, such as the evaporation rate of the two planets and their velocity and density atmospheric structure. We consider an atmosphere that is made only of Hydrogen, and the ionization balance is self-consistently derived by including Ly-alpha cooling and photoionization by XUV stellar irradiation (Allan & Vidotto 2019). To derive

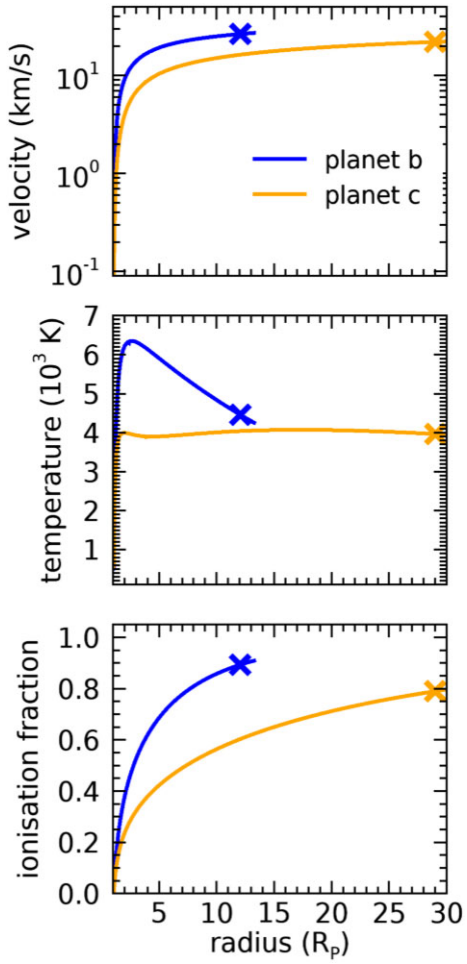

Figure 12. Atmospheric profiles derived from our hydrodynamic escape simulations showing the radial (i.e. outwards) velocity of the planetary outflow (top), its temperature (middle), and ionization fraction (bottom). The crosses indicate the radial distance to the Roche lobe. HD 73583 b and HD 73583 c properties are shown with blue and orange lines, respectively.

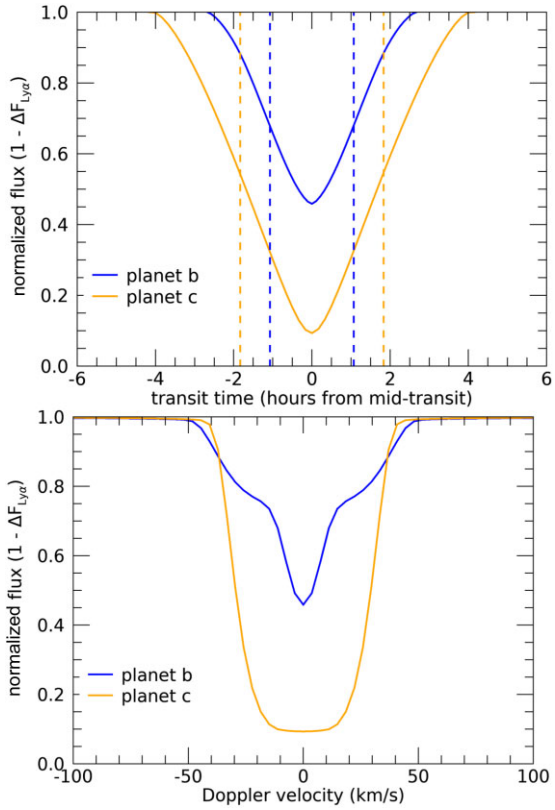

Figure 13. Top: Ly α light curves for planet HD 73583 b (blue) and HD 73583 c (orange). The dashed lines mark the duration of the geometric transit. Bottom: Normalized absorption profile at mid-transit for planet HD 73583 b (blue) and HD 73583 c (orange).

the XUV stellar flux, we proceed as follows. From the median value of HARPS $\log R'_{HK}$ (–4.465 ± 0.015), we calculated the Ca II H and K chromospheric emission flux using the equations in Fossati et al. (2017) and derived the XUV flux using the scaling relations of Linsky, France & Ayres (2013) and Linsky, Fontenla & France (2014). The corresponding stellar XUV luminosity is $9 \times 10^{-6}\ L_\odot$, which results in fluxes of 3.5×10^3 and 8.3×10^2 erg cm^{-2} s^{-1} at the orbital distance of planets b and c, respectively. Without knowledge of the SED in the X-ray and EUV bands, we assume this flux is concentrated at 20 eV as done in Allan & Vidotto (2019) (see also Hazra, Vidotto & D'Angelo 2020). The RV of the escaping atmosphere, temperature, and ionization fraction for both planets are shown in Fig. 12. The simulations are computed up to the Roche lobe (indicated by the crosses in Fig. 12). At these points, we see that the escaping atmospheres reach velocities between ∼20 and ∼30 km s^{-1}. These atmospheres are 50 per cent ionized at distances of ∼2.8 R_p and ∼7.4 R_p, for planets b and c, respectively. The 50 per cent threshold is achieved further out for planet c, because of the lower stellar flux it receives. We found evaporation rates for HD 73583 b of 2.4×10^{10} g s^{-1} and for HD 73583 c of 5.4×10^9 g s^{-1}.

From the neutral Hydrogen density, velocity and temperature profiles, we can predict the transit in Ly α and H α for both planets. This is done using a ray-tracing model (Vidotto et al. 2018; Allan & Vidotto 2019), in which we shoot stellar rays through the planetary atmosphere and we calculate how much of these rays are transmitted through the atmosphere. The top panel of Fig. 13 shows the predicted light curves at the Ly α line centre. We found a total absorption at mid-transit of 96 per cent for planet HD 73583 b and 52 per cent for planet HD 73583 c in Ly α. Although this is a strong absorption, we note from the bottom panel that this absorption is mostly concentrated in the line centre (i.e. not extending too much to the line wings), where observations are not possible due to ISM absorption and geocoronal contamination. Therefore, these estimations should be taken carefully. The reason for the large absorption at line centre is that our 1D hydrodynamic model cannot include 3D effects that could broaden the absorption. A broader absorption could be possible if we were to include the effect of the stellar wind in our escape models (Villarreal D'Angelo et al. 2018; Carolan et al. 2021) and other process like charge exchange and radiation pressure (Bourrier & Lecavelier des Etangs 2013; Khodachenko et al. 2017; Esquivel et al. 2019), which are out of the scope of this paper.

While most of the neutral Hydrogen is found in the ground state, a fraction of the atoms are in the first excited state ($n = 2$). These atoms can then absorb stellar H α photons, which could generate a detectable H α transit (Jensen et al. 2012, 2018; Casasayas-Barris et al. 2018; Cabot et al. 2020; Chen, Fan & Wang 2020; Yan et al. 2021).

To compute the level 2 population in the atmosphere of HD 73583 b and c, we follow the method described in Villarreal D'Angelo et al. (2021). We take as an input the electron density and the temperature

of the planetary atmosphere from the 1D hydrodynamic model and include the stellar Ly α flux as an external radiation field. This flux is approximated with a black-body function at a temperature of 8000 K (see also Christie, Arras & Li 2013; Huang et al. 2017). We then use our ray-tracing method and predict a small percentage of absorption during transit in H α, 0.32 per cent and 0.26 per cent for planets HD 73583 b and c, respectively. This low value of absorption is consistent with the fact that, so far, hot-Jupiter like exoplanets with H α absorption detection have $T_{\rm eq} > 1000$ K (Jensen et al. 2012, 2018; Chen et al. 2020) while both planets studied here show relatively small equilibrium temperatures.

6.4.3 Helium escape

We use a different 1D hydrodynamic escape model to estimate the absorption signatures that could be expected from HD 73583 b and HD 73583 c in the near-infrared line triplet of neutral helium at 1083 nm. The model assumes an atmosphere composed entirely of atomic Hydrogen and helium, in 9:1 number ratio. The density and velocity structures of the escaping atmosphere are based on the isothermal Parker wind model described in Oklopčić & Hirata (2018). For the input stellar spectrum used in our model, we construct a SED appropriate for HD 73583 (a K4-type star) by taking an average between the spectra of ϵ Eridani (K2 type) and HD 85512 (K6 type) obtained by the MUSCLES survey (France et al. 2016). We further adjust the high-energy part of the spectrum to match the expected XUV flux of HD 73583 at the orbital distances of the two planets. In addition to atmospheric composition, the main free parameters of the model are the temperature of the escaping atmosphere and the total mass-loss rate. We run a grid of models spanning a range of temperatures (3000–7000 K) and mass-loss rates (between $\dot{\rm M} = 10^{8}$ and $\dot{\rm M} = 10^{10.5}$ g s^{-1}). To calculate the abundance of helium atoms in the excited (metastable) state which is responsible for the 1083 nm absorption line, we perform radiative transfer calculations for a 1D atmospheric profile along the planet's terminator. We compute the transmission spectrum for a planet at mid-transit, assuming the planet is tidally locked and the atmosphere is rotating with the planet as a solid body.

The predicted signals for both planets are typically small, below 1 per cent excess absorption at the centre of the 1083 nm line. Fig. 14 shows the expected excess absorption at mid-transit for the mass-loss rates and temperatures similar to those predicted by the previously described Hydrogen simulations. We note that the 1D models used for simulating Hydrogen and helium signals use different assumptions and atmospheric profiles. Using the results of one model as input for the other is not entirely self-consistent, so these results should only be considered as rough estimates of the helium absorption signals from these two planets.

We note that while this paper was under review, Zhang et al. (2022) reported Helium detection in the atmosphere of HD 73583 b. This confirms the expected atmospheric evolution on this system and encourages further spectroscopic follow-up. A comparison of our results with their detection and models is out of the scope of this manuscript.

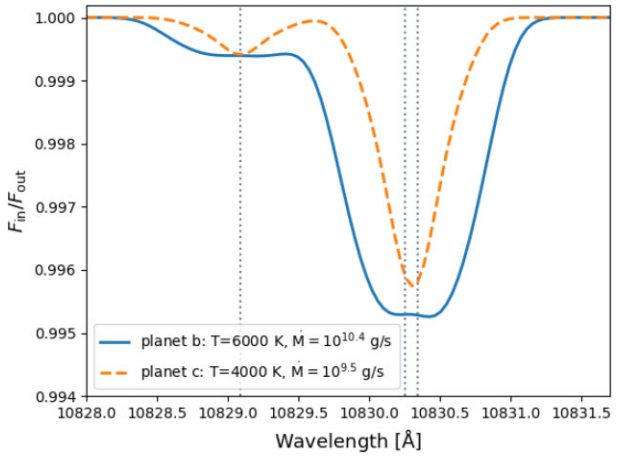

Figure 14. Calculated excess absorption at mid-transit in the helium 1083 nm line for HD 73583 b (solid blue line) and HD 73583 c (dashed orange line). The values of the input parameters are motivated by the results of the atmospheric escape simulations using pure Hydrogen composition. The dotted lines mark the wavelengths (in air) of the helium triplet lines.

ACKNOWLEDGEMENTS

This work was supported by the KESPRINT collaboration, an international consortium devoted to the characterization and research of exoplanets discovered with space-based missions (http://www.kesprint.science). We thank the referee for their helpful comments and suggestions that improved the quality of this manuscript. We acknowledge the use of public TESS data from pipelines at the TESS Science Office and at the TESS Science Processing Operations Center. Resources supporting this work were provided by the NASA High-End Computing (HEC) Program through the NASA Advanced Supercomputing (NAS) Division at Ames Research Center for the production of the SPOC data products. This work uses observations from the LCOGT network. Part of the LCOGT telescope time was granted by NOIRLab through the Mid-Scale Innovations Program (MSIP). MSIP is funded by NSF. This paper is in part based on data collected under the NGTS project at the ESO La Silla Paranal Observatory. The NGTS facility is operated by the consortium institutes with support from the UK Science and Technology Facilities Council (STFC) projects ST/M001962/1 and ST/S002642/1. This research has used the NASA Exoplanet Archive, which is operated by the California Institute of Technology, under contract with the National Aeronautics and Space Administration under the Exoplanet Exploration Program. Some of the observations in the paper used the High-Resolution Imaging instrument Zorro obtained under Gemini LLP Proposal Number: GN/S-2021A-LP-105. Zorro was funded by the NASA Exoplanet Exploration Program and built at the NASA Ames Research Center by Steve B. Howell, Nic Scott, Elliott P. Horch, and Emmett Quigley. Zorro was mounted on the Gemini North (and/or South) telescope of the international Gemini Observatory, a program of NSF's OIR Lab, which is managed by the Association of Universities for Research in Astronomy (AURA) under a cooperative agreement with the National Science Foundation on behalf of the Gemini partnership: the National Science Foundation (United States), National Research Council (Canada), Agencia Nacional de Investigación y Desarrollo (Chile), Ministerio de Ciencia, Tecnología e Innovación (Argentina), Ministério da Ciência, Tecnologia, Inovações e Comunicações (Brazil), and Korea Astronomy and Space Science Institute (Republic of Korea). OB, BK, and SA acknowledge that this publication is part of a project that has received funding from the European Research Council (ERC) under the European Union's Horizon 2020 research and innovation programme (Grant agreement No. 865624). DG and LMS gratefully acknowledge financial support from the *Cassa di Risparmio*

di Torino foundation under Grant No. 2018.2323 'Gaseous or rocky? Unveiling the nature of small worlds'. DJA acknowledges support from the STFC via an Ernest Rutherford Fellowship (ST/R00384X/1). APH and ME acknowledges grant HA 3279/12-1 within the DFG Schwerpunkt SPP 1992, 'Exploring the Diversity of Extrasolar Planets'. JS and PK would like to acknowledge support from MSMT grant LTT-20015. We acknowledges the support by FCT – Fundação para a Ciência e a Tecnologia through national funds and by FEDER through COMPETE2020 – Programa Operacional Competitividade e Internacionalização by these grants: UID/FIS/04434/2019; UIDB/04434/2020; UIDP/04434/2020; PTDC/FIS-AST/32113/2017 & POCI-01-0145-FEDER-032113; PTDC/FISAST /28953/2017 & POCI-01-0145-FEDER-028953. AD acknowledges the financial support of the European Research Council (ERC) under the European Union's Horizon 2020 research and innovation programme (project FOUR ACES; grant agreement No 724427). AD also acknowledges financial support of the the Swiss National Science Foundation (SNSF) through the National Centre for Competence in Research 'PlanetS'. MF, IYG, JK, and CMP gratefully acknowledge the support of the Swedish National Space Agency (DNR 177/19, 174/18, 2020-00104, 65/19). FGC thanks the Mexican national council for science and technology (CONACYT, CVU-1005374). MS acknowledge financial support of the Inter-transfer grant no LTT-20015. JL-B acknowledges financial support received from 'la Caixa' Foundation (ID 100010434) and from the European Union's Horizon 2020 research and innovation programme under the Marie Sklodowska-Curie grant agreement No 847648, with fellowship code LCF/BQ/PI20/11760023. AAV acknowledges funding from the European Research Council (ERC) under the European Union's Horizon 2020 research and innovation programme (grant agreement No 817540, ASTROFLOW). JMAM is supported by the National Science Foundation Graduate Research Fellowship Program under Grant No. DGE-1842400. JMAM acknowledges the LSSTC Data Science Fellowship Program, which is funded by LSSTC, NSF Cybertraining Grant No. 1829740, the Brinson Foundation, and the Moore Foundation; his participation in the program has benefited this work. RAR is supported by the NSF Graduate Research Fellowship, grant No. DGE 1745301. RL acknowledges financial support from the Spanish Ministerio de Ciencia e Innovación, through project PID2019-109522GB-C52, and the Centre of Excellence 'Severo Ochoa' award to the Instituto de Astrofísica de Andalucía (SEV-2017-0709). PC acknowledges the generous support from Deutsche Forschungsgemeinschaft (DFG) of the grant CH 2636/1-1. SH acknowledges CNES funding through the grant 837319. VA acknowledges the support from Fundação para a Ciência e Tecnologia (FCT) through Investigador FCT contract nr. IF/00650/2015/CP1273/CT0001. ODSD is supported in the form of work contract (DL 57/2016/CP1364/CT0004) funded by national funds through Fundação para a Ciência e Tecnologia (FCT). AO is supported by an STFC studentship. XD would like to acknowledge the funding from the European Research Council (ERC) under the European Union's Horizon 2020 research and innovation programme (grant agreement SCORE No 851555). HJD acknowledges support from the Spanish Research Agency of the Ministry of Science and Innovation (AEI-MICINN) under the grant 'Contribution of the IAC to the PLATO Space Mission' with reference PID2019-107061GB-C66, DOI: 10.13039/501100011033. DD acknowledges support from the TESS Guest Investigator Program grant 80NSSC19K1727 and NASA Exoplanet Research Program grant 18-2XRP18_2-0136. AO gratefully acknowledges support from the Dutch Research Council NWO Veni grant.

DATA AVAILABILITY

Some of the codes used in this manuscript are available as online supplementary material accessible following the links provided in the online version. Our spectroscopic measurements are available as a supplementary material in the online version of this manuscript.

REFERENCES

Acton J. S. et al., 2020, MNRAS, 498, 3115
Adams F. C., Laughlin G., 2006, ApJ, 649, 1004
Aigrain S., Pont F., Zucker S., 2012, MNRAS, 419, 3147
Allan A., Vidotto A. A., 2019, MNRAS, 490, 3760
Allard F., Homeier D., Freytag B., 2012, Phil. Trans. R. Soc. A, 370, 2765
Ambikasaran S., Foreman-Mackey D., Greengard L., Hogg D. W., O'Neil M., 2015, IEEE Trans. Pattern Anal. Mach. Intell., 38, 252
Angus R., Morton T. D., Foreman-Mackey D., 2019, J. Open Source Softw., 4, 1469
Armstrong D. J. et al., 2020, Nature, 583, 39
Baranne A. et al., 1996, A&AS, 119, 373
Barbary K., 2016, J. Open Source Softw., 1, 58
Barnes S. A., 2003, ApJ, 586, 464
Barragán O. et al., 2018, A&A, 612, A95
Barragán O., Gandolfi D., Antoniciello G., 2019, MNRAS, 482, 1017
Barragán O. et al., 2019, MNRAS, 490, 698
Barragán O., Aigrain S., Gillen E., Gutiérrez-Canales F., 2021, Res. Notes AAS, 5, 51
Barragán O., Aigrain S., Rajpaul V. M., Zicher N., 2022, MNRAS, 509, 866
Benz W. et al., 2021, Exp. Astron., 51, 109
Bertin E., Arnouts S., 1996, A&AS, 117, 393
Bouma L. G. et al., 2020, AJ, 160, 239
Bourrier V., Lecavelier des Etangs A., 2013, A&A, 557, A124
Bressan A., Marigo P., Girardi L., Salasnich B., Dal Cero C., Rubele S., Nanni A., 2012, MNRAS, 427, 127
Brown T. M. et al., 2013, PASP, 125, 1031
Bryant E. M. et al., 2020, MNRAS, 494, 5872
Cabot S. H. C., Madhusudhan N., Welbanks L., Piette A., Gandhi S., 2020, MNRAS, 494, 363
Cale B. L. et al., 2021, AJ, 162, 295
Carleo I. et al., 2020, AJ, 160, 114
Carolan S., Vidotto A. A., Plavchan P., Villarreal D'Angelo C., Hazra G., 2020, MNRAS, 498, L53
Carolan S., Vidotto A. A., Villarreal D'Angelo C., Hazra G., 2021, MNRAS, 500, 3382
Casasayas-Barris N. et al., 2018, A&A, 616, A151
Castelli F., Kurucz R. L., 2003, in Piskunov N., Weiss W. W., Gray D.F., eds, Proc. IAU Symp. 210, Modelling of Stellar Atmospheres. Kluwer, Dordrecht, p. A20
Chambers J. E., 1999, MNRAS, 304, 793
Chen Z., Fan J., Wang K., 2020, preprint (arXiv:2010.09830)
Choi J., Dotter A., Conroy C., Cantiello M., Paxton B., Johnson B. D., 2016, ApJ, 823, 102
Christie D., Arras P., Li Z.-Y., 2013, ApJ, 772, 144
Ciardi D. R., Beichman C. A., Horch E. P., Howell S. B., 2015, ApJ, 805, 16
Collins K. A., Kielkopf J. F., Stassun K. G., Hessman F. V., 2017, AJ, 153, 77
Collins K., Quinn S. N., Latham D. W., Christiansen J., Ciardi D., Dragomir D., Crossfield I., Seager S., 2018, in American Astronomical Society Meeting Abstracts, Vol. 231. p. 439.08
Crane J. D., Shectman S. A., Butler R. P., Thompson I. B., Birk C., Jones P., Burley G. S., 2010, in McLean I. S., Ramsay S. K., Takami H., eds, Proc.SPIE Conf. Ser. Vol. 7735, Ground-based and Airborne Instrumentation for Astronomy III. SPIE, Bellingham, p. 773553
Cutri R. M. et al., 2003, VizieR Online Data Catalog, II/246
da Silva L. et al., 2006, A&A, 458, 609
Delgado Mena E. et al., 2019, A&A, 624, A78

Dumusque X., Boisse I., Santos N. C., 2014, ApJ, 796, 132
Eisner N., Lintott C., Aigrain S., 2020, J. Open Source Softw., 5, 2101
Esposito M. et al., 2019, A&A, 623, A165
Esquivel A., Schneiter M., Villarreal D'Angelo C., Sgró M. A., Krapp L., 2019, MNRAS, 487, 5788
Faria J. P. et al., 2020, A&A, 635, A13
Foreman-Mackey D., Hogg D. W., Lang D., Goodman J., 2013, PASP, 125, 306
Fossati L. et al., 2017, A&A, 601, A104
France K. et al., 2016, ApJ, 820, 89
Fulton B. J. et al., 2017, AJ, 154, 109
Gaia Collaboration, 2018, VizieR Online Data Catalog, I/345
Gandolfi D. et al., 2018, A&A, 619, L10
Gandolfi D. et al., 2019, ApJ, 876, L24
Georgieva I. Y. et al., 2021, MNRAS, 505, 4684
Ginzburg S., Schlichting H. E., Sari R., 2016, ApJ, 825, 29
Gray R. O., Corbally C. J., Garrison R. F., McFadden M. T., Bubar E. J., McGahee C. E., O'Donoghue A. A., Knox E. R., 2006, AJ, 132, 161
Gregory P. C., 2005, ApJ, 631, 1198
Grunblatt S. K., Howard A. W., Haywood R. D., 2015, ApJ, 808, 127
Guerrero N. M. et al., 2021, ApJS, 254, 39
Gupta A., Schlichting H. E., 2019, MNRAS, 487, 24
Gupta A., Schlichting H. E., 2021, MNRAS, 504, 4634
Hatzes A. P. et al., 2010, A&A, 520, A93
Hatzes A. P. et al., 2011, ApJ, 743, 75
Haywood R. D. et al., 2014, MNRAS, 443, 2517
Hazra G., Vidotto A. A., D'Angelo C. V., 2020, MNRAS, 496, 4017
Hobson M. J. et al., 2021, AJ, 161, 235
Howard A. W. et al., 2010, ApJ, 721, 1467
Howell S. B., Everett M. E., Sherry W., Horch E., Ciardi D. R., 2011, AJ, 142, 19
Howell S. B., Everett M. E., Horch E. P., Winters J. G., Hirsch L., Nusdeo D., Scott N. J., 2016, ApJ, 829, L2
Hoyer S., Guterman P., Demangeon O., Sousa S. G., Deleuil M., Meunier J. C., Benz W., 2020, A&A, 635, A24
Huang C., Arras P., Christie D., Li Z.-Y., 2017, ApJ, 851, 150
Huélamo N. et al., 2008, A&A, 489, L9
Husser T. O., Wende-von Berg S., Dreizler S., Homeier D., Reiners A., Barman T., Hauschildt P. H., 2013, A&A, 553, A6
Isaacson H., Fischer D., 2010, ApJ, 725, 875
Jenkins J. M., 2002, ApJ, 575, 493
Jenkins J. M. et al., 2010, in Radziwill N. M., Bridger A., eds, Proc. SPIE Conf. Ser. Vol. 7740, Software and Cyberinfrastructure for Astronomy. SPIE, Bellingham, p. 77400D
Jenkins J. M. et al., 2016, in Chiozzi G., Guzman J. C., eds, Proc. SPIE Conf. Ser. Vol. 9913, Software and Cyberinfrastructure for Astronomy IV.. SPIE, Bellingham, p. 99133E
Jenkins J. M., Tenenbaum P., Seader S., Burke C. J., McCauliff S. D., Smith J. C., Twicken J. D., Chandrasekaran H., 2020, in Jenkins J. M., ed., Kepler Data Processing Handbook: Transiting Planet Search, Kepler Science Document KSCI-19081-003. p. 9
Jensen E., 2013, Astrophysics Source Code Library, record ascl:1306.007
Jensen A. G., Redfield S., Endl M., Cochran W. D., Koesterke L., Barman T., 2012, ApJ, 751, 86
Jensen A. G., Cauley P. W., Redfield S., Cochran W. D., Endl M., 2018, AJ, 156, 154
Kempton E. M. R. et al., 2018, PASP, 130, 114401
Khodachenko M. L. et al., 2017, ApJ, 847, 126
Kipping D. M., 2013, MNRAS, 435, 2152
Klein B. et al., 2021, MNRAS, 502, 188
Kossakowski D. et al., 2021, A&A, 656, A124
Kubyshkina D., Lendl M., Fossati L., Cubillos P. E., Lammer H., Erkaev N. V., Johnstone C. P., 2018, A&A, 612, A25
Kupka F., Piskunov N., Ryabchikova T. A., Stempels H. C., Weiss W. W., 1999, A&AS, 138, 119
Kurucz R. L., 1993, SYNTHE Spectrum Synthesis Programs and Line Data
Lester K. V. et al., 2021, AJ, 162, 75
Li J., Tenenbaum P., Twicken J. D., Burke C. J., Jenkins J. M., Quintana E. V., Rowe J. F., Seader S. E., 2019, PASP, 131, 024506
Lightkurve Collaboration, 2018, Astrophysics Source Code Library, record ascl:1102.027
Lillo-Box J. et al., 2020, A&A, 640, A48
Linsky J. L., France K., Ayres T., 2013, ApJ, 766, 69
Linsky J. L., Fontenla J., France K., 2014, ApJ, 780, 61
Lopez E. D., Fortney J. J., 2014, ApJ, 792, 1
Lovis C., Pepe F., 2007, A&A, 468, 1115
Lundkvist M. S. et al., 2016, Nat. Commun., 7, 11201
Mamajek E. E., Hillenbrand L. A., 2008, ApJ, 687, 1264
Mandel K., Agol E., 2002, ApJ, 580, L171
Mann A. W. et al., 2017, AJ, 153, 64
Mann A. W. et al., 2022, AJ, 163, 156
Martioli E., Hébrard G., Correia A. C. M., Laskar J., Lecavelier des Etangs A., 2021, A&A, 649, A177
Maxted P. F. L. et al., 2011, PASP, 123, 547
Mayor M. et al., 2003, The Messenger, 114, 20
Mazeh T., Holczer T., Faigler S., 2016, A&A, 589, A75
McCully C., Volgenau N. H., Harbeck D.-R., Lister T. A., Saunders E. S., Turner M. L., Siiverd R. J., Bowman M., 2018, in Guzman J. C. Ibsen J., eds, Proc. SPIE Conf. Ser. Vol. 10707, Software and Cyberinfrastructure for Astronomy V. SPIE, Bellingham, p. 107070K
Miller-Ricci E., Seager S., Sasselov D., 2009, ApJ, 690, 1056
Mordasini C., 2020, A&A, 638, A52
Morton T. D., 2015, Astrophysics Source Code Library, record ascl:1503.010.
Newton E. R. et al., 2019, ApJ, 880, L17
Newton E. R. et al., 2021, AJ, 161, 65
Nielsen L. D. et al., 2020, MNRAS, 492, 5399
Niraula P. et al., 2017, AJ, 154, 266
Oklopčić A., Hirata C. M., 2018, ApJ, 855, L11
Osborn A. et al., 2021, MNRAS, 507, 2782
Owen J. E., Wu Y., 2013, ApJ, 775, 105
Pepe F., Mayor M., Galland F., Naef D., Queloz D., Santos N. C., Udry S., Burnet M., 2002, A&A, 388, 632
Piskunov N., Valenti J. A., 2017, A&A, 597, A16
Piskunov N. E., Kupka F., Ryabchikova T. A., Weiss W. W., Jeffery C. S., 1995, A&AS, 112, 525
Plavchan P. et al., 2020, Nature, 582, 497
Pollacco D. L. et al., 2006, PASP, 118, 1407
Queloz D. et al., 2001a, The Messenger, 105, 1
Queloz D. et al., 2001b, A&A, 379, 279
Rajpaul V., Aigrain S., Osborne M. A., Reece S., Roberts S., 2015, MNRAS, 452, 2269
Rajpaul V., Aigrain S., Roberts S., 2016, MNRAS, 456, L6
Raymond S. N., Barnes R., Veras D., Armitage P. J., Gorelick N., Greenberg R., 2009, ApJ, 696, L98
Ricker G. R. et al., 2015, J. Astron. Telesc. Instrum. Syst., 1, 014003
Rizzuto A. C. et al., 2020, AJ, 160, 33
Russell D. G., 2021, preprint (arXiv:2108.03343)
Santos N. C. et al., 2013, A&A, 556, A150
Schlegel D. J., Finkbeiner D. P., Davis M., 1998, ApJ, 500, 525
Smith J. C. et al., 2012, PASP, 124, 1000
Smith A. M. S. et al., 2020, Astron. Nachr., 341, 273
Sneden C. A., 1973, PhD thesis, Univ. Texas at Austin
Sousa S. G., 2014, in Determination of Atmospheric Parameters of B. p. 297
Sousa S. G., Santos N. C., Israelian G., Mayor M., Monteiro M. J. P. F. G., 2007, A&A, 469, 783
Sousa S. G., Santos N. C., Adibekyan V., Delgado-Mena E., Israelian G., 2015, A&A, 577, A67
Sousa S. G. et al., 2021, A&A, 656, A53
Southworth J., Wheatley P. J., Sams G., 2007, MNRAS, 379, L11
Stassun K. G. et al., 2018, AJ, 156, 102
Stassun K. G. et al., 2019, AJ, 158, 138
Stumpe M. C. et al., 2012, PASP, 124, 985
Stumpe M. C., Smith J. C., Catanzarite J. H., Van Cleve J. E., Jenkins J. M., Twicken J. D., Girouard F. R., 2014, PASP, 126, 100
Szabó G. M. et al., 2021, A&A, 654, A159
Teske J. et al., 2021, ApJS, 256, 33
Thompson A. P. G., Watson C. A., de Mooij E. J. W., Jess D. B., 2017, MNRAS, 468, L16

Twicken J. D. et al., 2018, PASP, 130, 064502
Van Eylen V., Agentoft C., Lundkvist M. S., Kjeldsen H., Owen J. E., Fulton B. J., Petigura E., Snellen I., 2018, MNRAS, 479, 4786
Vidotto A. A. et al., 2018, MNRAS, 481, 5296
Villarreal D'Angelo C., Esquivel A., Schneiter M., Sgró M. A., 2018, MNRAS, 479, 3115
Villarreal D'Angelo C., Vidotto A. A., Esquivel A., Hazra G., Youngblood A., 2021, MNRAS, 501, 4383
Wheatley P. J. et al., 2018, MNRAS, 475, 4476
Winn J. N., 2010, preprint (arXiv:1001.2010)
Wright E. L. et al., 2010, AJ, 140, 1868
Yan F. et al., 2021, A&A, 645, A22
Yee S. W., Petigura E. A., von Braun K., 2017, ApJ, 836, 77
Zeng L., Sasselov D. D., Jacobsen S. B., 2016, ApJ, 819, 127
Zeng L. et al., 2019, Proc. Natl. Acad. Sci., 116, 9723
Zhang M., Knutson H. A., Wang L., Dai F., Barragán O., 2022, AJ, 163, 67
Zhou G. et al., 2021, AJ, 161, 2

SUPPORTING INFORMATION

Supplementary data are available at *MNRAS* online.

Table B1. HARPS spectroscopic measurements.
Table B2. HIRES spectroscopic measurements.
Table B3. CORALIE spectroscopic measurements.

Please note: Oxford University Press is not responsible for the content or functionality of any supporting materials supplied by the authors. Any queries (other than missing material) should be directed to the corresponding author for the article.

APPENDIX A: CORRELATION PLOT

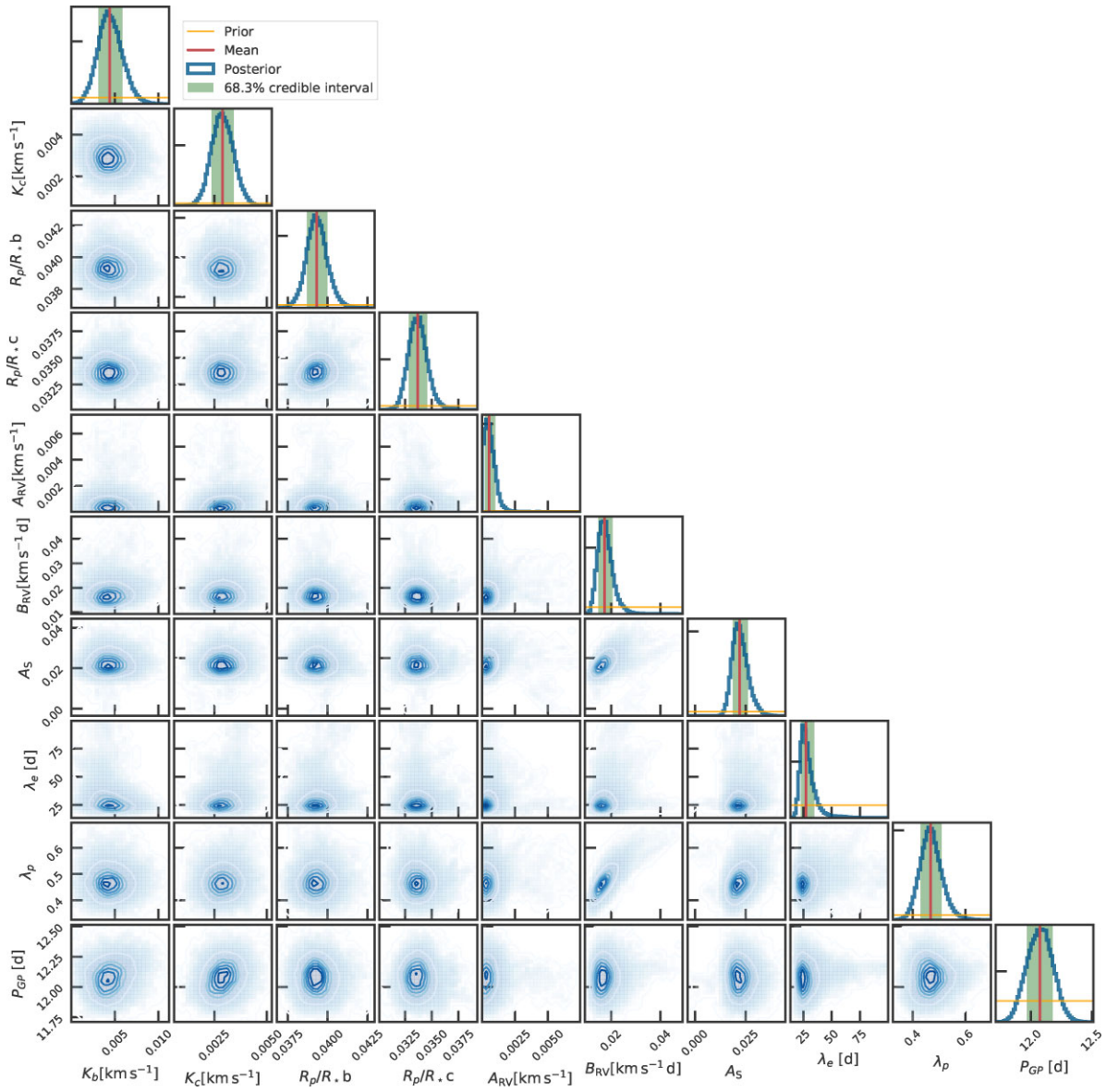

Figure A1. Posterior andcorrelation plots for some of the key sampled parameters of the joint analysis described in Section 5.3.

APPENDIX C: GP TESTS

In this appendix, we show some further tests that we perform in order to understand the modelling of the stellar and planetary signals in our spectroscopic time-series.

C1 Stellar and planetary signals in the RV time-series only

We first make an analysis of the RV time-series to test if we can detect the planetary signals without a multi-GP approach. We perform a one-dimensional GP regression using the QP kernel given in equation 2. For the GP model we sampled for only one amplitude and the QP kernel hyper-parameters. The Keplerian deterministic part of our model is identical to the one described in Section 5. Our MCMC set-up follows is identical to the description in Section 5.3.

We recover the hyper-parameters $P_{\rm GP} = 12.11^{+0.08}_{-0.09}$ d, $\lambda_{\rm p} = 0.24^{+0.04}_{-0.03}$, and $\lambda_{\rm e} = 24^{+4}_{-3}$ d. We note that the $P_{\rm GP}$ and $\lambda_{\rm e}$ are consistent with the values obtained in the joint analysis. However, $\lambda_{\rm p}$ is significantly smaller. This relative high harmonic complexity in the RV time-series is expected as we discussed at the beginning of Section 6.1 and in Barragán et al. (2022).

The recovered planetary signals are $3.52^{+1.45}_{-1.41}$ m s^{-1} and 2.63 ± 0.68 m s^{-1} for HD 73583 b and c, respectively. We can see that these results are consistent with the values obtained in Section 5.3. However, the results obtained with the multi-GP have better constrained values (see Table 4). This improvement in the detection in the multi-GP analysis comes from a better constrain on the the underlying function $G(t)$ with help of the activity indicator (For a more extensive discussion about this see Barragán et al. 2022).

C2 Stellar signal in the $S_{\rm HK}$ time-series

We also perform a one-dimensional GP regression to the $S_{\rm HK}$ time-series for all the instrument. This with the objective to see if we are able to recover the stellar signal purely with the activity indicator itself. For the GP model we sampled for only one amplitude and the QP kernel hyper-parameters. We also sampled for an independent offset and jitter term per each spectrograph. Our MCMC set-up follows the same guidelines as the previous cases. We recover the hyper-parameters $P_{\rm GP} = 12.22^{+0.33}_{-0.45}$ d, $\lambda_{\rm p} = 0.62^{+0.20}_{-0.14}$ and $\lambda_{\rm e} = 31^{+12}_{-09}$ d, and GP amplitude of $0.031^{+0.007}_{-0.005}$. These are consistent with the results obtained in Section 5. This shows that the $S_{\rm HK}$ time-series by itself can constrain the $G(t)$ function describing the stellar signal.

It is worth to note that the recovered $P_{\rm GP}$ and $\lambda_{\rm e}$ in this section and in Appendix C1 are fully consistent. This suggests that the stellar rotation period and spot typical lifetime manifest with the same time-scales in RV and $S_{\rm HK}$ observations. In contrast, the inverse of the harmonic complexity is significantly different in both cases. This shows how the RV and photometric-like activity indicators are not described by the same $G(t)$ signal (but they all can be described as linear combinations of a single $G(t)$ its time derivatives).

We note that the residuals of the $S_{\rm HK}$ time-series in Fig. 7 present some significant variations. We penalize this in our model with the jitter terms. But this implies that our model may not be perfect describing our data. This can be caused by instrumental systematics that we are not taking into account, and by the limitation of assuming that the stellar signal can be described with a GP. However, as we show in this section, our model is enough to constrain the stellar signal at a first order.

C3 Tests with other activity indicators

As a further check of our modelling of our stellar activity signal, we perform extra tests using DRS CCF activity indicators for our HARPS data. The Pearson correlation coefficient between RVs with FWHM, $S_{\rm HK}$ and BIS are –0.16, 0.18, and –0.70, respectively. From the correlation analysis, one may think that the best activity indicator to use is the BIS span. However, it is worth to note that the stellar activity does not manifest as the same signal in the different time-series (see e.g. Dumusque et al. 2014). Some activity indicators, such as FWHM and $S_{\rm HK}$, depend only on the projected area of the active regions on the stellar surface, similar to photometric signals. We refer to these activity indicators as photometric-like (for more details see Isaacson & Fischer 2010; Thompson et al. 2017). While other quantities such as RV and BIS span are also sensitive to the change of location of the active regions from the red- to the blue-shifted stellar hemisphere, and vice versa (for a more detailed discussion about this see e.g. Aigrain et al. 2012; Rajpaul et al. 2015; Barragán et al. 2022). Therefore, given that the BIS span and RVs depend in a similar way on the stellar activity, it is expected that they present a strong correlation. Therefore, we do not consider correlation between RVs and activity indicators a good proxy to choose the best activity indicator for a multi-GP analysis.

What we are interested in the multi-GP approach is to find an activity indicator that help us to constrain better the $G(t)$ variable. We therefore perform a similar analysis to the one presented in Section 5.2 but we use FWHM instead of using the $S_{\rm HK}$ to constrain the shape of the $G(t)$ function. The recovered Keplerian and hyper-parameters are in full agreement with the values reported in Section 5. This is expected given that we foresee that FWHM and $S_{\rm HK}$ constrain the shape of the $G(t)$ function.

We also performed a three-dimensional GP regression including the RV, FWHM, and BIS time-series. We assume that the BIS span is described by a linear combination of $G(t)$ and $\dot{G}(t)$ (As originally presented by Rajpaul et al. 2015). Our model set-up follows the same guidelines described in Section 5.2. As in the previous case, the recovered and Keplerian and hyper-parameters are consistent with the main analysis described in Section 5. It is worth to mention that for this case we did not see an improvement in the determination of the planetary parameters. This implies that the extra complexity to the model added with the inclusion of the BIS time-series does not help to constrain better the shape of $G(t)$ in this particular data set.

These results give us confidence that our model to describe the stellar signal in the RV and activity time-series is reliable for this case. We note that we use the $S_{\rm HK}$ time-series in our final model because it is an activity indicator that is independent of the RV extraction method therefore it is available for all the instruments.

[1]*Sub-department of Astrophysics, Department of Physics, University of Oxford, Oxford OX1 3RH, UK*
[2]*Department of Physics, University of Warwick, Coventry CV4 7AL, UK*
[3]*Centre for Exoplanets and Habitability, University of Warwick, Coventry CV4 7AL, UK*
[4]*Dipartimento di Fisica, Università degli Studi di Torino, Via Pietro Giuria 1, I-10125 Torino, Italy*
[5]*Department of Astronomy, Indiana University, Bloomington, IN 47405, USA*
[6]*Leiden Observatory, Leiden University, PO Box 9513, NL-2300 RA Leiden, the Netherlands*
[7]*Instituto de Astronomía Teórica y Experimental (CONICET - UNC). Laprida 854, X500 BGR. Córdoba, Argentina*
[8]*Anton Pannekoek Institute for Astronomy, University of Amsterdam, Science Park 904, NL-1098 XH Amsterdam, the Netherlands*

[9]*501 Campbell Hall, University of California at Berckeley, Berkeley, CA 94720, USA*
[10]*Department of Physics and Astronomy, University of New Mexico, 1919 Lomas Blvd NE, Albuquerque, NM 87131, USA*
[11]*Center for Astrophysics | Harvard & Smithsonian, 60 Garden Street, Cambridge, MA 02138, USA*
[12]*Department of Earth and Space Sciences, Chalmers University of Technology, Onsala Space Observatory, SE-439 92 Onsala, Sweden*
[13]*Instituto de Astrofísica e Ciências do Espaço, Universidade do Porto, CAUP, Rua das Estrelas, P-4150-762 Porto, Portugal*
[14]*Astrophysics Group, Keele University, Staffordshire ST5 5BG, UK*
[15]*NASA Ames Research Center, Moffett Field, CA 94035, USA*
[16]*Astronomy Department and Van Vleck Observatory, Wesleyan University, Middletown, CT 06459, USA*
[17]*Department of Space, Earth and Environment, Astronomy and Plasma Physics, Chalmers University of Technology, SE-412 96 Gothenburg, Sweden*
[18]*Geneva Observatory, University of Geneva, Chemin Pegasi 51, CH-1290 Versoix, Switzerland*
[19]*Department of Astronomy, California Institute of Technology, Pasadena, CA 91125, USA*
[20]*Carnegie Earth & Planets Laboratory, 5241 Broad Branch Road, NW, Washington, DC 20015, USA*
[21]*SETI Institute, Mountain View, CA 94043, USA*
[22]*Thüringer Landessternwarte Tautenburg, Sternwarte 5, D-07778 Tautenberg, Germany*
[23]*Mullard Space Science Laboratory, University College London, Holmbury St Mary, Dorking, Surrey RH5 6NT, UK*
[24]*European Southern Observatory, Alonso de Cordova 3107, 7630391 Vitacura, Santiago de Chile, Chile*
[25]*Departamento de Física e Astronomia, Faculdade de Ciências, Universidade do Porto, Rua do Campo Alegre, P-4169-007 Porto, Portugal*
[26]*Department of Astronomy and Astrophysics, University of California, Santa Cruz, CA 95064, USA*
[27]*Centro de Astrobiología (INTA-CSIC), Camino Bajo del Castillo s/n, E-28692 Villanueva de la Cañada, Madrid, Spain*
[28]*Department of Physics, and Institute for Research on Exoplanets, Université de Montréal, Montreal, QC H3T 1J4, Canada*
[29]*Jet Propulsion Laboratory, California Institute of Technology, 4800 Oak Grove Drive, Pasadena, CA 91109, USA*
[30]*Institute of Planetary Research, German Aerospace Center, Rutherfordstrasse 2, D-12489 Berlin, Germany*
[31]*School of Physics and Astronomy, University of Leicester, University Road, Leicester LE1 7RH, UK*
[32]*McDonald Observatory and Center for Planetary Systems Habitability, University of Texas, Austin, TX 78712 USA*
[33]*Carnegie Observatories, 813 Santa Barbara Street, Pasadena, CA 91101, USA*
[34]*Department of Physics and Astronomy, University of Kansas, Lawrence, KS 66045, USA*
[35]*European Space Agency (ESA), European Space Research and Technology Centre (ESTEC), Keplerlaan 1, NL-2201 AZ Noordwijk, the Netherlands*
[36]*George Mason University, 4400 University Drive, Fairfax, VA 22030 USA*
[37]*Department of Physics and Kavli Institute for Astrophysics and Space Research, Massachusetts Institute of Technology, Cambridge, MA 02139, USA*
[38]*Department of Astrophysical Sciences, Peyton Hall, 4 Ivy Lane, Princeton, NJ 08544, USA*
[39]*Instituto de Astrofísica de Canarias, E-38205 La Laguna, Tenerife, Spain*
[40]*Departamento de Astrofísica, Universidad de La Laguna, E-38206 La Laguna, Spain*
[41]*European Southern Observatory, Alonso de Cordova, Vitacura, Santiago, Chile*
[42]*NASA Exoplanet Science Institute, Caltech/IPAC, Mail Code 100-22, 1200 E. California Blvd., Pasadena, CA 91125, USA*
[43]*Departamento de Astronomía, Universidad de Guanajuato, Callejón de Jalisco s/n 36023, México*
[44]*Gemini Observatory/NSF's NOIRLab, 670 N. A'ohoku Place, Hilo, HI 96720, USA*
[45]*Astrobiology Center, 2-21-1 Osawa, Mitaka, Tokyo 181-8588, Japan*
[46]*National Astronomical Observatory of Japan, NINS, 2-21-1 Osawa, Mitaka, Tokyo 181-8588, Japan*
[47]*Aix Marseille Univ, CNRS, CNES, LAM, F-13013 Marseille, France*
[48]*Astronomical Institute of the Czech Academy of Sciences, Fričova 298, CZ-25165 Ondřejov, Czech Republic*
[49]*Centro de Astrobiología (CAB, CSIC-INTA), Depto. de Astrofísica, ESAC campus, E-28692 Villanueva de la Cañada (Madrid), Spain*
[50]*Instituto de Astrofísica de Andalucía (IAA-CSIC), Glorieta de la Astronomía s/n, E-18008 Granada, Spain*
[51]*NCCR/PlanetS, Centre for Space & Habitability, University of Bern, CH-3012 Bern, Switzerland*
[52]*Hazelwood Observatory, Churchill, Victoria, Australia*
[53]*Patashnick Voorheesville Observatory, Voorheesville, NY 12186, USA*
[54]*Department of Theoretical Physics and Astrophysics, Masaryk University, Kotlárská 2, CZ-61137 Brno, Czech Republic*
[55]*Astronomical Institute of Charles University, V Holešovičkách 2, CZ-180 00 Prague, Czech Republic*
[56]*Perth Exoplanet Survey Telescope, 337 Walnut Rd, Bickley WA 6076, Australia*
[57]*Curtin Institute of Radio Astronomy, Curtin University, Bentley, Western Australia 6102, Australia*
[58]*Astrophysics Research Centre, School of Mathematics and Physics, Queen's University Belfast, BT7 1NN Belfast, UK*
[59]*Department of Astronomy, Tsinghua University, Beijing 100084, People's Republic of China*
[60]*Seniors Data Scientist, SiteZeus*
[61]*Department of Physics, Engineering and Astronomy, S. F. Austin State University, 1936 North St, Nacogdoches, TX 75962, USA*

This paper has been typeset from a TEX/LATEX file prepared by the author.